Oxygen atom kinetics in CO2 plasmas ignited in a DC glow discharge

A. S Morillo-Candas, Cyril Drag, Jean-Paul Booth, T. C Dias, V. Guerra, Olivier Guaitella

Oxygen atom kinetics in CO_2 plasmas ignited in a DC glow discharge

A.S. Morillo-Candas[1,*], C. Drag[1], J.-P. Booth[1], T.C. Dias[2], V. Guerra[2], O. Guaitella[1]

[1] *Laboratoire de Physique des Plasmas (UMR 7648), CNRS-Univ.Paris Sud-Sorbonne Université-École polytechnique 91128 Palaiseau, France*

[2] *Instituto de Plasmas e Fusão Nuclear, Instituto Superior Técnico, Universidade de Lisboa 1049-001 Lisboa, Portugal*

(*) ana-sofia.morillo-candas@lpp.polytechnique.fr

Abstract

Oxygen atom densities were measured *in situ* in a CO_2 glow discharge, at pressures between 0.2 and 5 Torr (26.7-666.6 Pa). Two measurement techniques were compared, namely optical emission actinometry (using Ar as the actinometer) and High-Resolution Two-photon Absorption Laser Induced Fluorescence (HR-TALIF) normalised to Xe, and were found to give consistent results. The variation of the atomic oxygen density with gas pressure shows two different regimes with a transition around 1 Torr. Measurements of the O atom loss frequency under plasma exposure showed that this behaviour is caused by a change in the O atom loss mechanisms, which are dominated by surface processes in our experimental conditions. The corresponding recombination probabilities on Pyrex γ_O are found to vary with the gas temperature near the wall for a constant surface temperature, similarly to what has recently been obtained in pure O_2. However, the measured values are more than two times lower than γ_O obtained in a O_2 plasma in similar conditions. The O atom densities are also compared to the dissociation fraction of CO_2 determined by infra-red absorption. The obtained CO and O densities show different behaviour as a function of the energy input. The simultaneous measurement of gas temperature, electric field, O, CO and CO_2 densities and O atoms loss frequency in the same conditions provides an ideal set of constraints for validating CO_2 plasma kinetic models.

1 Introduction

The increasing concentration of CO_2 in the atmosphere due to anthropogenic emissions is widely established to be a major cause of climate change [1]. This is motivating the development of different strategies to reduce the emissions of CO_2 or to capture and store it from industrial sources. An attractive possibility is to recycle CO_2 as a raw material for the synthesis of more complex organic molecules, such as energy-dense hydrocarbon fuels. The use of low temperature plasmas has potential to increase the overall efficiency of this process, and is compatible with the use of intermittent renewable energy sources.

The dissociation to CO is the first step in plasma conversion of CO_2. The so-called vibration up-pumping of the asymmetric-stretch vibrational mode of CO_2 has been proposed to be the most efficient path [2]. Many different plasma sources have been investigated over a large range of pressures: from 10 to 1000 Pa with DC glow or radio frequency discharges [3–6], from few kPa to tens of kPa with RF and microwave discharges [7–10], at atmospheric pressure with gliding arc [11, 12], dielectric barrier discharges [13–15] or micro-hollow cathode discharges [16] or even above atmospheric pressure with nanosecond discharges [17, 18]. These plasma sources and others have been listed and compared in terms of conversion efficiency in several review articles [19–21]. Other applications of CO_2 plasmas include polymer deposition at low pressure [22–24], planetary atmosphere entry studies [25–30] and oxygen production from the Martian atmosphere composed of almost pure CO_2 at a few hundreds of Pa [4, 31, 32].

The dissociation of CO_2 produces O atoms, which will then undergo further reactions which can have beneficial or detrimental impact in the final conversion. On the one hand, they can react with vibrationally excited CO_2 [2, 33], increasing the dissociation. On the other

hand O atoms can quench the vibrational excitation of CO_2 [34–36] or oxidize CO back to CO_2. Oxygen atoms can also simply recombine into O_2. They play therefore an important but complex role in CO_2 plasma dynamics and on the efficiency of CO_2 conversion.

The role of oxygen atoms in CO_2 plasmas, although essential, remains poorly documented. Most of the available papers deal with spacecraft entry into the atmospheres of Mars or Venus, from both experimental [37–39] and modelling [26, 27, 40] points of view. These studies are usually performed with large gas flows and with gas temperatures between 1000 to 4000 K, which is too high to take advantage of non-equilibrium conditions [2]. Some papers in the field of CO_2 lasers have briefly discussed the role of O atoms but mainly from modelling point of view [41, 42] and often with CO_2 being largely diluted in mixing with N_2 and He [36, 43, 44]. The vibrational quenching coefficient by O atoms is reported only for the very first vibrational level of the asymmetric stretch mode $CO_2(001)$ with significant discrepancies [34, 45]; the quenching of higher levels, when taken into account, is only extrapolated from a first order perturbation theory [46] and no experimental data are available. Another example is the reaction of O with vibrationally excited CO_2 to produce CO + O_2, which is reported in models, however its rate coefficient depending on vibrational levels has not been measured and is also extrapolated [33]. Similarly, the oxidation reaction of CO to CO_2 is only well documented for ground state O and CO, but not for excited states.

In addition to the importance of oxygen atoms in gas phase processes, surface processes involving atomic oxygen can also be very important for the use of CO_2 plasmas. Indeed, one of the possible approaches to improve the efficiency of CO_2 conversion consists of coupling the plasma with adsorbent and/or catalysts [47–49]. When using these materials in contact with the plasma, oxygen atoms can either recombine into O_2 or O_3, or possibly react on the surface with CO or CO_2 molecules. Surface reactions in CO_2 plasmas, and in particular of oxygen atoms, are still poorly known even on surfaces as simple as SiO_2. While the loss probability of O atoms has been extensively studied in pure O_2 plasma, very few data are reported in CO_2 plasma, mostly for atmospheric entry [26, 40] and polymer treatment at very low pressure [50]. An additional difficulty is that afterglow data can not be used to study the surface kinetics under direct plasma exposure. For instance, it has been shown in pure O_2 that surface loss mechanisms can be enhanced up to two orders of magnitude when surfaces are under direct plasma exposure [51, 52]. In addition, the few available experimental data are often difficult to interpret because of the complexity of the processes induced in a CO_2 plasma and the difficulty to isolate the different mechanisms involved.

This paper is part of a recent effort to investigate different aspects of the kinetics of CO_2 plasmas and disentangle the underlying elementary processes. We have chosen to use as plasma source a DC glow discharge, which is simple, reproducible and homogeneous (in the positive column). It allows therefore the joint use of multiple complementary diagnostic methods, in order to separate the important mechanisms influencing CO_2 plasma kinetics. The low pressure range, in addition to its relevance for some applications, has the advantage of allowing easier monitoring of the evolution of different processes due to the slower characteristic times. This experimental approach can then be used as a basis for validating kinetic models and the knowledge acquired is essential to optimise the actual discharges to be used in future applications. Following this approach, we previously measured the vibrational temperatures of CO_2 and CO in a pulsed DC discharge for different pressures (1-5 Torr) and currents (10-50 mA) [53, 54]. These first measurements showed a good agreement with a kinetic model describing the vibrational kinetics of CO_2 under conditions of very low dissociation rate (pulsed plasma at low repetition rate) in which the quantities of CO and O can be neglected [55, 56]. A more complete description of the kinetics of CO_2 plasmas requires now a deeper investigation of the interactions between CO_2, CO and atomic oxygen.

In this work we investigate the kinetics of O atoms in similar discharge conditions as in our previous works [53–57] with two main purposes. The first objective is to determine accurately the absolute O atom densities under conditions where the CO_2 and CO densities are also well characterized. To the best of our knowledge, absolute densities of CO_2 and CO and O together have never been measured *in situ* at the same plasma conditions. We measured the absolute atomic oxygen density at pressures in the range 0.2 - 5 Torr (26.7-666.6 Pa) and discharge currents from 10 to 50 mA using both actinometry and High Resolution-Two photon Absorption Laser Induced Fluorescence (HR-TALIF). Each of these commonly used techniques have advantages and limitations that are discussed in detail to assess the level of accuracy of the absolute values obtained. FTIR absorption spectroscopy was used to determine the density of CO and CO_2 in the discharge, and thus the dissociation rate.

The second objective is to investigate the main O atom loss mechanisms in our conditions. We determine the O atoms loss frequency under direct plasma exposure using a time-resolved actinometry technique in partial modu-

lated discharges developed by Lopaev *et al.* [58]. This technique has been recently used in pure O_2 plasma showing that the O atom loss frequency passes through a minimum with pressure [59]. Notice that in our experimental conditions the O atom loss processes are *a priori* dominated by surface recombination at the reactor walls. Our approach insures the surface to be continuously exposed to plasma and therefore allows the determination of the surface loss probability in the active discharge. However, at the highest pressures studied, gas phase losses must be also considered and discussed.

The different experimental set-ups used for actinometry, HR-TALIF and FTIR measurements are presented in the next section. In section 3, the principles of actinometry and TALIF are briefly reviewed and the choices made to analyse the data are described. Section 4 presents measurements of parameters including the gas temperature and electric field, which are essential for both control of the plasma conditions, and analysis of actinometry and TALIF data. Section 5 presents the results of CO and O atom absolute densities and recombination probabilities with an assessment of their accuracy, before discussing them in section 6. Finally, section 7 summarises the main results and closes the paper.

2 Experimental set-up

2.1 Discharge reactor

The CO_2 glow discharge was ignited in a 2 cm inner-diameter cylindrical Pyrex tube. Two different reactor lengths were used, 67 cm for TALIF and actinometry and 23 cm for *in situ* FTIR experiments. The tube is double-walled, allowing control of the wall temperature by circulating a mixture of distilled water and ethanol at a temperature fixed at 323K (50^0C) for all experiments. The discharge was established between two cylindrical metallic electrodes located in perpendicular side tubes, 17 or 53 cm apart, depending on the tube length. This configuration ensures that IR absorption measurements (line-of sight-integrated) are taken only through the positive column of the glow discharge. The anode was connected to a DC high voltage power supply through a 68 kΩ non-inductive ballast resistor.

The pressure in the tube was varied between 0.2 and 5 Torr, with a constant total gas flow of 7.4 sccm (set by Brooks SLA5850S1 or Bronkhorst F-201CV flow controllers) using gas from bottles of pure CO_2, O_2, Ar and Xe (Air Liquide Alphagaz 1 for CO_2 and Ar, and Alphagaz 2 for O_2 and Xe). The pressure was measured with a capacitance manometer (Pfeiffer CMR263/ MKS 122AA), and the gas was evacuated by a scroll pump (Edwards, XDS35) through a pressure-regulating valve (Pfeiffer EVR116 + controller RVC300). The discharge current was varied between 10 and 50 mA, working either in continuous or in partial-modulation regimes (see details of the latter in section 2.3). The axial electric field was determined from the voltage drop between two tungsten probes, located 20 cm apart in the long discharge tube. All measurements were taken at the axial centre of the positive column of the glow discharge; radial gradients in the electric field were therefore not taken into account.

2.2 HR-TALIF setup

The laser set-up used for HR-TALIF measurements (shown schematically in figure 1), uses a commercial single-mode continuous Titanium:Sapphire (Ti:Sa) laser (Coherent MBR 110 pumped by a 10W Verdi Nd:YVO_4 laser) to seed a home-built nanosecond pulsed ring cavity Ti:Sa laser, pumped by a 20Hz 532nm Nd:YAG laser (Quantel CFR200) [60–63]. The seed laser is injected co-linearly with the pump laser into a Ti:Sa crystal. The cavity also contains two prisms to coarsely select the output wavelength range with a spectral resolution of about 15 cm^{-1}. The cavity is locked to the frequency of the seed laser by adjusting the cavity length using a piezoelectric actuator on one of the mirrors, in order to operate the ring cavity in a single longitudinal mode. The wavelength of the seed laser is monitored by a wave-meter (Angstrom WSU from High Finesse, measurement resolution 5MHz FWHM).

The output pulses from the ring laser (at around 903 nm) are then frequency-doubled twice by non-linear BBO crystals, generating ultraviolet pulses around 225.6 nm with an energy of approximately 1 mJ. The spectral width of the ultraviolet pulses is around 0.006 cm^{-1} FHWM, close to the Fourier transform limit of the pulse duration. The ultraviolet beam is spatially separated from the longer-wavelength components using a fused silica Pellin-Broca prism and passed through a home-made attenuator (allowing the laser energy to be varied without changing the spatio-temporal profile), towards the long discharge tube, which is closed with two CaF_2 windows. The beam was not focused (the reason for this is explained below). The laser pulse duration is approximately 7.5 ns and a reflection from a mirror/beam splitter was monitored with a fast UV photo-diode to trigger the data acquisition. After exiting the tube, the beam is reflected by a dielectric mirror at 45^0 (97% of the laser energy) towards a laser energy meter (Sensor PE10-C + controller Pulsar, Ophir). Behind this last mirror we installed an IR photo-diode with

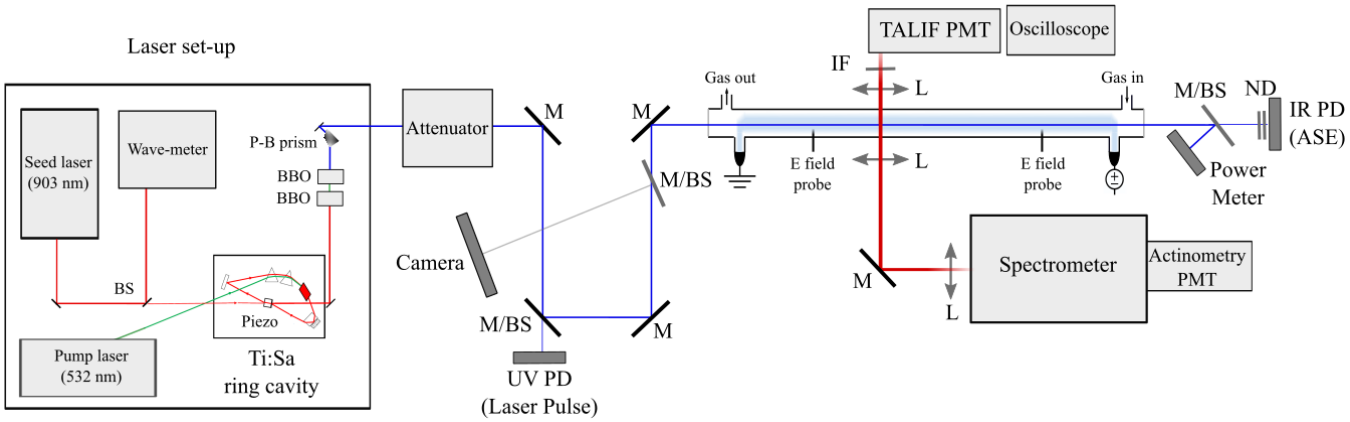

Figure 1: Experimental set-up used (non-simultaneously) for TALIF and actinometry experiments. M: Mirror, BS: Beam splitter, L: Lens, PD: Photo-diode, PMT: Photomultiplier, IF: Interference filter, ND: Neutral density filter. The laser set-up is shown with a simplified version of the optics.

two neutral density filters in order to detect the onset of the amplified spontaneous emission (ASE) signal from the transmitted (IR) light. All TALIF data was recorded using a laser energy below the threshold for ASE.

The fluorescence from the laser-excited atoms at 844.6 nm was collected perpendicularly to the laser beam by a f=35.5 mm lens, imaged onto a horizontal slit, passed through an interference filter (840 nm centre wavelength, 13 nm FWHM), and detected with a photomultiplier (Hamamatsu R13456, with a time response of 2.7 ns) fitted with a gated voltage-divider circuit (Hamamatsu C1392-56) to avoid saturation by the plasma emission. The fluorescence signal, the laser pulse signal (UV photo-diode) and the ASE signal (IR photo-diode) were monitored with a digital oscilloscope (LeCroy HDO4104). A Labview program was used to record the fluorescence intensity, the laser energy and the seed laser wavelength. The laser beam profile was measured with a camera beam profiler (Thorlabs BC106N) and the beam waist was derived assuming a Gaussian spatial profile.

2.3 Actinometry set-up

The atomic oxygen (777.4 and 844.6 nm, hereinafter O777 and O845) and argon (750.4 nm, Ar750) emission intensities were collected perpendicular to the reactor axis (see figure 1), by a collimating lens with the focal point at the centre of the discharge tube. The collimated beam was steered by mirrors and focused into the entrance slit of a spectrometer (Princeton Isoplane STC-320). The light at the output slit was detected with an IR-sensitive photomultiplier (Hamamatsu H7422-50) and recorded by a data acquisition card (National Instruments NI-USB-6210). The fraction of argon in the total gas mixture was kept constant at 5% in order to minimize its effect on the CO_2 plasma dynamics. For time-resolved actinometry experiments, the discharge current was partially modulated using a circuit between the cathode and the ground comprising a 15 kΩ resistor in parallel with a transistor switch. A Labview program was used to record the intensity of the emission lines, along with the plasma current, voltage and electric field and their evolution over time.

The wavelength dependence of the relative sensitivity of the full optical detection system was calibrated for the three emission lines used for actinometry. The infrared output of the single-mode continuous Ti:Sa described above was directed through the discharge tube following the same optical path as the light emitted by the plasma. The power of the laser was attenuated by using several beam splitters, and a diffuser (Thorlabs) was used to reproduce a diffuse light source. The diffused light was focussed into the entrance slit of the spectrometer. The response of the beam splitters and the diffuser was checked, and showed the same response for the three wavelengths studied. With no plasma in the discharge tube, and using constant laser power, the relative intensities of the signals obtained at each wavelength were recorded, providing two correction factors ($I_{O777}/I_{Ar} = 1.44$ and $I_{O845}/I_{O777} = 3.20$) that were applied to the actinometry formula (see section 3.1.1).

2.4 FTIR set-up

The *in situ* FTIR measurements were performed with the short plasma reactor (23 cm length) positioned in the sample chamber of an FTIR spectrometer (Bruker, Vertex 70), with a spectral resolution of 0.2 cm^{-1}. The FTIR was operated in conventional mode, averaging 20 scans. In

order to obtain the final absorption spectrum, two complementary measurements were performed: an absorption measurement, taken with the infra-red source of the interferometer on, and an emission measurement performed with the infra-red source off, in order to record the plasma emission spectrum. This emission is reflected towards the interferometer and subsequently reabsorbed by the plasma, being therefore spectrally resolved. The emission spectrum is subtracted from the absorption spectrum and the final transmittance is obtained by dividing the remainder by the spectral profile of the IR source. The obtained spectra are fitted with a MATLAB script described in [53]. Downstream measurements were also performed by passing the effluent from the discharge through a measurement cell situated in the sample compartment of the FTIR, in order to check that the dissociation fractions obtained with both long and short plasma reactors are similar for a given gas residence time.

3 O atom density measurements

3.1 Actinometry

3.1.1 Principles

Actinometry is a widely used emission spectroscopy technique described extensively in literature and originally developed for atomic fluorine [64]. Here, we only recall its main characteristics to discuss the accuracy of the atomic oxygen density values obtained and compared them to HR-TALIF measurements. With actinometry, the density of a reactive species of interest is determined from the ratio of the intensity of emission from an excited state of the probed species to that from a rare gas (actinometer), which is added in small amount to the gas mixture. It assumes that the observed emitting electronically excited states are predominantly populated by electron impact from the ground state. In this case, the observed emission intensity is given by [65]:

$$I_X = C_X \cdot h\nu_{ij}^X \cdot k_e^X \cdot n_e \cdot \frac{A_{ij}^X}{\sum A_i^X + \sum_Q k_Q^X [n_Q]} [n_X] \qquad (1)$$

where C_X is a constant dependent on the detection system, in our case calculated with the calibration factors described in section 2.3, $h\nu_{ij}$ is the energy of the emitted photons, n_e is the electron density and $[n_X]$ is the density of the atoms in the ground state. k_e^X is the excitation rate coefficient, calculated with the expression [66]:

$$k_e^X = \left(\frac{2e}{m}\right)^{1/2} \int_{\varepsilon_{th}}^{\infty} \sigma_i(\varepsilon) f(\varepsilon) \varepsilon d\varepsilon \qquad (2)$$

where $\sigma_i(\varepsilon)$ is the collision cross section with threshold energy ε_{th} for the excitation of the level i and $f(\varepsilon)$ is the electron energy distribution function (EEDF), normalized by $\int_0^\infty f(\varepsilon)\varepsilon^{1/2} d\varepsilon = 1$. The effective branching ratio is:

$$a_{ij}^X = \frac{A_{ij}^X}{\sum_i A_i^X + \sum_Q k_Q^X [n_Q]} \qquad (3)$$

This term represents the ratio of the detected emission to the sum of all de-excitation processes, where A_{ij}^X is the Einstein coefficient for the measured transition and $\sum A_i^X$ is the sum over all the possible radiative de-excitation processes. The ratio $A_{ij}^X / \sum A_i^X$ is the pure optical branching ratio. $k_Q^X[n_Q]$ represents the non-radiative de-excitation processes, where k_Q^X is the rate coefficient for collisional quenching by species Q of density $[n_Q]$. In the case of oxygen-containing plasmas, dissociative excitation can also be a significant source of emitting atoms. This can be taken into account by substituting the term $k_e^X[n_X]$ in equation (1) by $k_e^X[n_X] + k_{de}^O[O_2]$, where k_{de}^O is calculated with equation (2) with the corresponding cross section. Rearranging the different terms and using argon as actinometer, the O atom density can be obtained from the expression [67]:

$$[O] = \frac{I_O}{I_{Ar}} \frac{C_{Ar} \cdot h\nu_{ij}^{Ar}}{C_O \cdot h\nu_{ij}^O} \frac{k_e^{Ar}}{k_e^O} \frac{a_{ij}^{Ar}}{a_{ij}^O} \cdot [Ar] - \frac{k_{de}^O}{k_e^O} [O_2] \qquad (4)$$

where the last term in equation (4) represents the contribution of dissociative excitation. Therefore, the calculation includes excitation through electron impact and dissociative excitation of O_2 by electron collisions, along with radiative and non-radiative (quenching) de-excitation processes.

3.1.2 Data and calculations

The cross sections used to calculate the excitation rate coefficients for direct electron impact and dissociative excitation for oxygen were taken respectively from Laher [68] and Schulman [69], and for the electron impact excitation of argon were taken from Puech [70]. These cross sections were chosen since they were found by Pagnon *et al.* [65] to give the best agreement between actinometry and VUV measurements for pure O_2 plasma. The EEDF was calculated using the two term approximation Boltzmann solver BOLSIG+ [66] and cross sections obtained from IST-Lisbon database for CO_2, O_2, O and Ar, available in LxCat [71], and for CO [72]. The experimental values of CO_2 dissociation (see section 5.1) were used to define the CO_2 and CO fractions for the calculation of the EEDF.

The Einstein coefficient values used in equation (3) were taken from the NIST database [73]: $A_{ij}^{O^3P} = 3.22 \times 10^7\, s^{-1}$, $A_{ij}^{O^5P} = 3.69 \times 10^7\, s^{-1}$, $A_{ij}^{Ar} = 4.45 \times 10^7\, s^{-1}$. The optical branching ratio $A_{ij}^X / \sum A_i^X$ is equal to 1 for oxygen and to 0.994 for argon [74]. The rate coefficients for quenching of the emitting oxygen states by O_2 molecules used here were [67] $K_Q^{O^3P} = 9.4 \times 10^{-16}\, m^3 s^{-1}$ [75], $K_Q^{O^5P} = 10.8 \times 10^{-16}\, m^3 s^{-1}$ [76]. These coefficients were measured in pure O_2 with an average error around 10%. However, other sources report significantly different values (*e.g.* $K_{O_2}^{O^3P} = 7.8 \times 10^{-16}\, m^3 s^{-1}$ [76]). To the best of our knowledge, there is no data available for the quenching of atomic oxygen lines by CO_2, CO or O. Therefore, we assumed these species have the same quenching rate coefficients as for O_2. We checked the validity of this assumption by measuring the decay time of the TALIF fluorescence signal while varying the gas mixture between pure CO_2 and pure O_2 (discussed in section 4.3). $[n_Q]$ was considered in this case equal to the total gas density (justified also in section 4.3). In the case of the Ar line, values are available for other quenchers: CO_2: $K_{CO_2}^{Ar\,2P_1} = 6.2 \times 10^{-16}\, m^3 s^{-1}$, CO: $K_{CO}^{Ar\,2P_1} = 1.1 \times 10^{-16}\, m^3 s^{-1}$ and O_2: $K_{O_2}^{Ar\,2P_1} = 7.6 \times 10^{-16}\, m^3 s^{-1}$ [77].

The density of O_2 used in equation (4) was assumed to be equal to half of the CO density determined with FTIR, *i.e.* the O_2 density that would be obtained if all the O atoms were recombined into molecular oxygen, which could lead to an overestimation of the dissociative excitation term. However, since the excitation rate coefficients for this process are at least two orders of magnitude smaller than the rate coefficients for direct excitation, the contribution of this term was found to be negligible.

In order to record the actinometry signal, the wavelength of the spectrometer is fixed at the peak of intensity of every emission line. Therefore, in principle, we should include a term to account for the Doppler broadening (and pressure broadening if needed), which reduces the intensity peak value, as it is done for HR-TALIF (see section 3.2.2) [78]. However in actinometry measurements the instrumental broadening is dominant, and the Doppler effect is negligible in comparison.

3.2 TALIF

3.2.1 Principles

Contrary to actinometry, Two-photon Absorption Laser Induced Fluorescence (TALIF) directly probes the atoms in their ground state [75, 79, 80]; these are pumped by the absorption of laser light to an electronically-excited state, which decays radiatively, emitting the detected fluorescence photons. We used the conventional TALIF scheme in which O atoms in the ground state are excited by two photons at 225.65 nm, emitting a fluorescence signal through the $3p\,^3P_J \rightarrow 3s\,^3S^o$ transitions at 844.6 nm. The relation between the ground state density and the detected signal is given, for a collimated beam (confocal parameter $\gg$ fluorescence viewing region) by the expression [81]:

$$N_{h\nu} = \frac{a_{ij}^X \cdot C_X\, \hat{\sigma}_X^{(2)} L\, E^2 \cdot n_X}{\pi \cdot w^2 \cdot (h\nu)^2} \cdot \int_{-\infty}^{\infty} F^2(t)dt \qquad (5)$$

where $N_{h\nu_i}$ is the fluorescence signal ($\sim$ total number of fluorescence photons), a_{ij}^X is the effective branching ratio described in equation (3), C_X is a constant dependent on the detection system, $\hat{\sigma_X}^{(2)}$ is the two-photon absorption cross section, L is the effective length of the light-collection system, E is the laser energy, w is the beam waist, n_X is the ground state density and $\int_{-\infty}^{\infty} F^2(t)dt$ is the integral of the temporal profile of the laser pulse.

In order to deduce absolute densities, we followed the calibration process first proposed by Goehlich *et al.* [82] and further developed by Niemi *et al.* [75]. This method is based on a reference measurement with a noble gas of known concentration, performed ideally with the same spatial, spectral, and temporal intensity distribution of the laser radiation, removing the necessity to know these distributions explicitly. This condition is best fulfilled if the two-photon resonances are spectrally close. Accordingly, xenon is commonly used as calibration gas to measure O atom densities [82]. Two possible Xe fluorescence transitions have been used in the literature for the calibration of O atom density, $6p'[3/2]_2 \rightarrow 6s'[1/2]_1$ and $7p[3/2]_2 \rightarrow 6s[3/2]_2$. We used the first one, which is excited by 224.31 nm photons and emits fluorescence at 834.91 nm. The term $\int_{-\infty}^{\infty} F^2(t)dt$ is similar for the measurements of O atom and Xe (the maximum difference was determined to be less than 8%). After normalizing the signal by the square of the laser pulse energy $S_X \sim N_{h\nu}^X / E^2$, the O atom density is deduced from the following expression [75]:

$$n_{O_{atom}} = \left[\frac{T_{Xe}}{T_O} \cdot \frac{\xi_{Xe}}{\xi_O} \cdot \frac{\sigma_{Xe}^{(2)}}{\sigma_O^{(2)}} \cdot \frac{a_{Xe}}{a_O} \cdot \frac{S_O}{S_{Xe}} \cdot \frac{w_O^2}{w_{Xe}^2} \cdot \frac{(h\nu_O)^2}{(h\nu_{Xe})^2}\right] \cdot \left[\frac{1}{n_{J=2}/\sum_J n_J}\right] \cdot n_{Xe} \qquad (6)$$

where T_X is the transmittance of the windows and ξ_X is the sensitivity of the detection system ($C_X = T_X \cdot \xi_X$), including the spectral responses of the photomultiplier (measured similarly as described in section 2.3) and of the interference filter (obtained from the data-sheet), for both

wavelengths. $\sigma^{(2)}_{Xe}/\sigma^{(2)}_{O}$ is the ratio of the two-photon absorption cross sections. To our knowledge, the Xe two-photon absorption cross section has not been published. Therefore we used the value of the ratio of both cross sections $\sigma^{(2)}_{Xe}/\sigma^{(2)}_{O} = 1.9$ determined by Niemi *et al.* [75], based on a titration method, with an estimated uncertainty ~20%. However, recent preliminary, direct, measurements of the Xe two-photon absorption cross section [83], seem to indicate that this value could be over-estimated, and point towards a $\sigma^{(2)}_{Xe}$ value smaller by a factor ~ 2 than the value determined by titration. The impact of this cross section on the final O atom density results will be discussed in section 5.2. The fluorescence quantum yield, a_{Xe}/a_{O}, was defined above in equation (3). The pure optical branching ratio $A^X_{ij}/\sum A^X_i$ is 1 for oxygen, while for Xe it is 0.733 [84, 85]. In the case of Xe, the radiative decay rate and quenching coefficient were taken from Niemi *et al.* [75] and are, respectively, $A_{Xe} = 2.45 \times 10^7\ s^{-1}$ and $k^{Xe}_q = 3.6 \times 10^{-10}\ cm^3 s^{-1}$. The density of Xe, n_{Xe}, in the discharge tube was calculated from the pressure and temperature with the ideal gas law. In the case of oxygen, a single effective quenching coefficient was used, therefore the total gas density was used as the quencher density (see section 4.3).

S_O/S_{Xe} is the experimentally observed ratio of the fluorescence, integrated either over time, for the TALIF fluorescence ratio, or over time and wavelength, for the TALIF excitation profile ratio (see section 3.2.2), and normalized to the squared laser energy, for the two species. Although ideally the beam spatial profile should be identical in the O and Xe measurements, in practice when the laser wavelength is varied, the position of the beam in the frequency doubling crystals changes slightly, affecting the beam shape. According to equation (5), the size of the beam must be taken into account and the term w^2_O/w^2_{Xe} in equation (6) represents the ratio of the laser beam waist diameters estimated using the laser beam profiler in the respective cases. ν_i is the frequency of the absorbed photons. Finally, the ground state of oxygen comprises three fine structure components, but we only determine the absolute density by TALIF in the level J=2; therefore we must include a term accounting for the fraction of O atoms in this level. We assume the fine-structure components are described by a Boltzmann distribution and are in equilibrium with the gas temperature. Consequently, the fraction of O atoms in the level J=2 is given by:

$$\frac{n_J}{\sum_J n_J} = \frac{(2J+1)\cdot \exp\left(-E_J/k_B \cdot T_g\right)}{\sum_J (2J+1)\cdot \exp\left(-E_J/k_B \cdot T_g\right)} \qquad (7)$$

which is equal to 0.67 for oxygen at 1 Torr 40 mA ($T_{gas} \approx 500\,K$), the condition for which the absolute calibration was made.

3.2.2 Measurement procedure

All TALIF data were obtained without focusing the laser beam. In initial measurements we did focus the beam, but we found that the two-photon absorption excitation line profile was distorted; the intensity ratio of the three fine-structure components of the upper O $3p\,^3P^J$ state did not match the theoretical values [86], and wide "wings" appeared. Possible origins of these effects include J-dependent photo-ionization of the emitting state, and production of hot O atoms by photo-dissociation of vibrationally-excited O_2 [75, 87]. Without laser focusing these effects disappeared. The quadratic dependence of the TALIF signal on the laser pulse energy was also verified, since any deviation from this dependence would indicate a significant perturbation by photo-ionization and/or amplified stimulated emission (ASE), leading to errors in the determined O atom density. The laser energy threshold for ASE was detected with the IR photo-diode as the laser energy was varied and, during subsequent measurements, the power of the laser was always kept below this threshold. For all TALIF data, laser shots where the laser energy fell below 75% of the average were rejected since they correspond to a failure of the cavity seeding.

For the absolute calibration, the excitation wavelength was scanned at a fixed laser pulse energy, for both gases. An example of the excitation spectra obtained from the integral of the TALIF fluorescence over time is shown in figure 2. As can be seen, the high spectral resolution of the laser allows us to partially resolve the fine structure of the excited level O ($3p\,^3P$); the contributions of the levels J=1 (88630.59 cm^{-1}, fluorescence transition $3p\,^3P_{J=1} \rightarrow 3s\,^3S_{J=1}$) and J=2 (88631.15 cm^{-1}, transition $3p\,^3P_{J=2} \rightarrow 3s\,^3S_{J=1}$) are easily distinguished. The J=0 (88631.30 cm^{-1}) contribution is weaker and convoluted with that from J=2 one [88]. In the conditions studied in this work, these profiles are dominated by Doppler broadening (*i.e.* pressure broadening, natural line-width and laser line-width are negligible), and can be fitted with a sum of three Gaussian functions to determine the temperature of the O atoms. The ratio of the TALIF signals, S_O/S_{Xe} in equation (6) is in this case simply the ratio of the TALIF signals integrated over time and wavelength and normalized to the laser intensity squared for both species *i.e.* an integral of the TALIF profiles shown in figure 2.

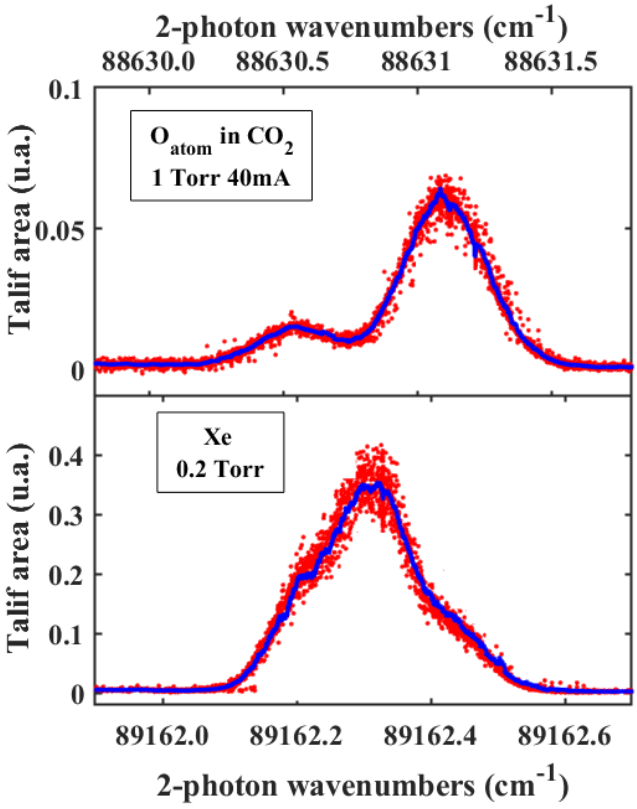

Figure 2: TALIF excitation profile for O atoms in a CO_2 plasma and for Xe. In red the raw data points, in blue the smoothed data (averaging 50 points) used for the integral calculation.

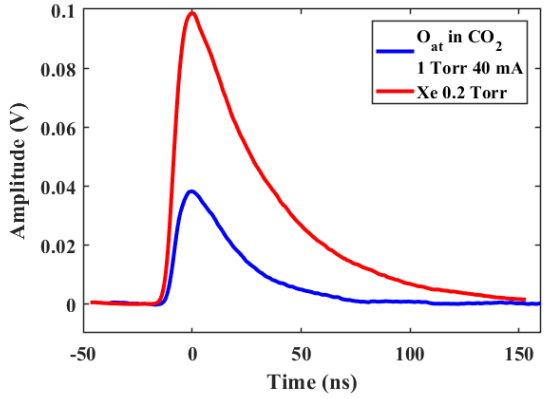

Figure 3: TALIF fluorescence signal over time for O atoms in CO_2 at 1 Torr 40 mA (transition $3p\ ^3P_{J=2} \rightarrow 3s\ ^3S_{J=1}$), and Xe at 0.2 Torr. The profile is an average over 300 laser shots.

The absolute calibration can also be achieved by recording only the TALIF fluorescence signal as a function of time, with the laser wavelength set to the maximum of the signal (at the peak of the resonance). An example is shown in figure 3, recorded by the oscilloscope and averaged over 300 laser shots. This signal must be corrected for the Doppler broadening, which reduces the signal at the peak. In the case of Xe, we take into account the contribution of the different isotopes by including a correction factor equal to 0.54 [89, 90]. Therefore, in this case, S_O/S_{Xe} in equation (6) is the ratio of the TALIF fluorescence signal, not integrated over wavelength but only over time, corrected for the Doppler broadening and the isotope contribution and normalized to the laser energy squared. The values of the absolute O atom densities obtained by this method were within 11% of the densities found by integrating over the complete TALIF excitation profile, and the data acquisition is much faster, being less affected by possible instabilities of the laser, and reducing the uncertainties caused by fluctuations in the laser beam spatial profile when scanning over wavelength. Therefore the measurements of the relative variation of the O atom density as a function of discharge parameters (pressure and current) were subsequently determined just from the signal at the peak wavelength corresponding to the transition $3p\ ^3P_{J=2} \rightarrow 3s\ ^3S_{J=1}$, corrected also for the quenching, as follows from equation (6). The transition $3p\ ^3P_{J=1} \rightarrow 3s\ ^3S_{J=1}$ was found to be give consistent O atom relative variation with pressure and current, finding a difference lower than 4%, which means that both transitions can be indifferently used to assess the variation of O atom density for different plasma parameters.

The temporal shape of the fluorescence signal is a convolution of the laser pulse duration (around 7.5 ns), the time response of the PMT (2.7 ns) and the lifetime of the fluorescing state. In order to evaluate the lifetime of the exited states (and therefore compensate for quenching in the calculation), we reject the first 7.5 ns after the peak (15 ns in total) to avoid any influence of the laser profile or the response of PMT in the fitting of the fluorescence decay. Concerning the integral of the TALIF fluorescence signal to obtain the absolute density, the effect of the response time of the PMT (assuming a Gaussian profile and convolving it with the exponential decay of the TALIF signal) gives an error in the integral below 0.5% for both O and Xe. The maximum effect of the laser pulse duration, also assuming a Gaussian profile, is around 3.5%; therefore both contributions were considered negligible. The laser beam shape, which is close to a gaussian profile, was recorded after each TALIF profile scan for absolute calibration in order to obtain the beam waist. For Xe $w^Y_{Xe} \approx 916.6\ \mu m$ and $w^X_{Xe} \approx 1083.8\ \mu m$ while for oxygen $w^Y_O \approx 892.1\ \mu m$ and $w^X_O \approx 733.5\ \mu m$.

4 Gas temperature, electric field and quenching coefficients

The gas temperature and the electric field are two essential parameters required for a good description of the CO_2 plasma kinetics. The gas temperature was determined independently by two diagnostic techniques, HR-TALIF and infra-red absorption. The consistency and accuracy of both is discussed in this section. The electric field is also needed to calculate the excitation coefficients necessary for actinometry. The temporal decay of the TALIF fluorescence signal allows the quenching rate of excited O atoms to be measured as a function of the gas mixture, which is necessary for the analysis of actinometry data.

4.1 Gas temperature

The rotational temperature of CO_2 (T_{rot}) was obtained by fitting the FTIR absorption spectra [53]. The translational temperature of the O atoms was obtained by fitting the Doppler broadening of the TALIF profile [60]. Figure 4 a) shows the variation of both with current and pressure. The temperatures obtained by the two techniques are very comparable, and therefore T_{rot} can be assumed to be in equilibrium with the gas temperature and confirms that O atoms and CO_2 molecules are in thermal equilibrium in our conditions. T_{gas} increases with both current and pressure. This can be explained by the higher power dissipated in the plasma as the current is increased, and the higher voltage (and therefore power) required to maintain the current as the pressure is increased. This dependence is clear when plotting T_{gas} *versus* the energy input, as shown in figure 4 b). This figure shows an almost linear increase of the gas temperature with the specific energy input (SEI), which is calculated from the discharge power dissipated in the positive column (see section 4.2) divided by the molecular flow, and takes into account the residence time of the gas in the plasma. The exact mechanisms responsible for the conversion of electrical energy into gas heating are complex, but could include enhanced V-T transfers at higher pressure, and possible exothermic reactions [91].

Beyond the good agreement between the temperatures obtained by FTIR and HR-TALIF, looking in more detail, the temperatures obtained with TALIF tend to be slightly higher than those obtained with FTIR. This difference increases with pressure and current and can be explained by the radial temperature gradient in the discharge tube, measured with TALIF (see section 6). The gas temperature at the centre of the tube and the radial gradients increase with pressure and current. The laser beam used for TALIF is relatively small, therefore TALIF measures the temperature at the tube axis (the hottest point). In contrast, the infra-red beam used for FTIR measurements is larger, filling the radius of the tube and the temperature obtained is an average over the radial profile of the discharge tube. Therefore, TALIF technique tends to give slightly higher values than FTIR at high pressure and current. For the following calculations, the temperature obtained with TALIF is used to obtain O atom densities from the TALIF signal, whereas the rotational temperature obtained by FTIR was used for FTIR, actinometry and to obtain the reduced electric field.

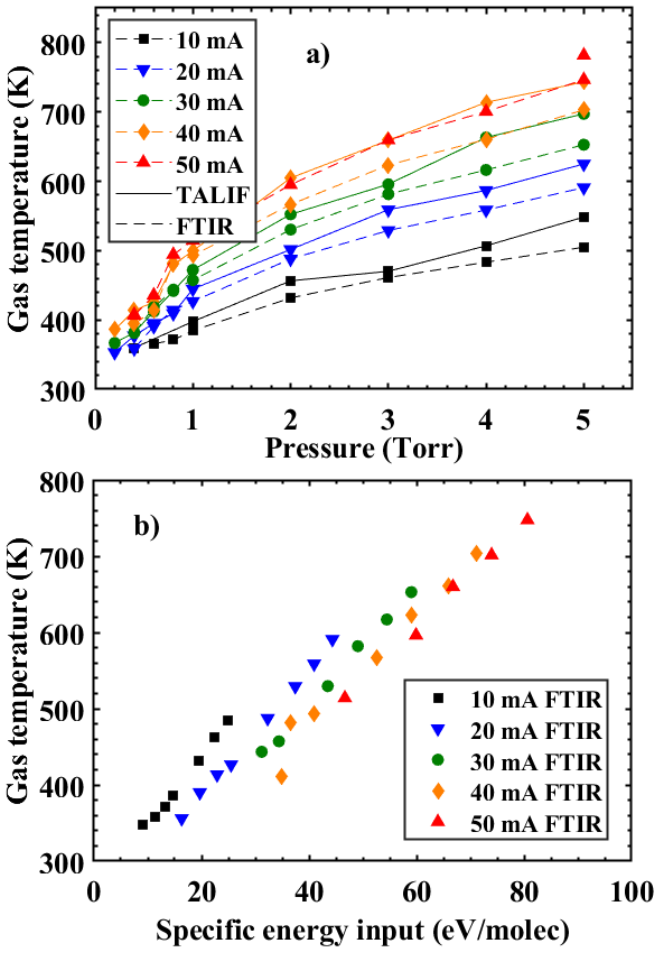

Figure 4: Gas temperature variation a) *versus* pressure for different currents obtained from the FTIR spectra (rotational temperature of CO_2) and from the Doppler broadening of TALIF signal (translational temperature of O atoms) and b) as a function of the specific energy input (SEI).

4.2 Electric field

The axial electric field was obtained from the voltage drop across the positive column of the glow discharge between the two tungsten probes, as described in section 2.1. The measured values and the corresponding reduced electric field, are shown versus gas density in figure 5. A single monotonous dependence with gas density is observed for all currents and pressures measured. As expected, a higher field is required to sustain the plasma when the gas density is higher, but the reduced electric field is smaller. For a given current, the reduced electric field decreases with pressure (opposite trend to the electric field), whereas at a given pressure the reduced field increases with current due to the effect of gas heating on the gas density. The power dissipated in the positive column can be calculated from the electric field and the discharge current. This power differs from the total power feeding the discharge due to the power dissipated in regions such as the cathode fall [92], which do not contribute significantly to the total dissociation. This has been verified by downstream FTIR measurements performed with the two discharge tubes (different length), which gave the same dissociation rate as a function of residence time.

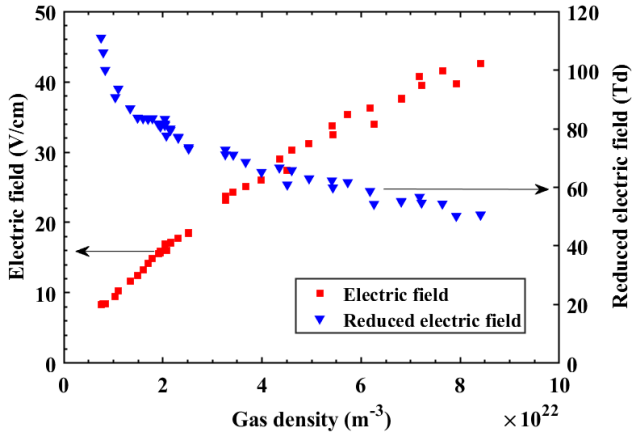

Figure 5: Variation of the electric field (left axis) and reduced electric field (right axis) as a function of the gas density for all pressure and current conditions of fig 4.

4.3 Quenching

Measurements of the temporal decay of the TALIF fluorescence signal after the laser pulse (such as shown in figure 3), give the effective decay rate of the O atoms in the exited state, which is related to the quenching rate coefficients by the expression:

$$A^* = \frac{1}{\tau^*} = \frac{1}{\tau_0} + \sum_Q k_Q[n_Q] \Rightarrow A^* = \sum_i A_i^X + \sum_Q k_Q[n_Q] \quad (8)$$

where A^* is the measured effective decay rate, τ^* is the effective lifetime, τ_0 is the natural lifetime accounting for all the possible radiative de-excitation processes, k_Q is the quenching coefficient and $[n_Q]$ is the density of quenchers. The experimental values of the effective decay rate, A^*, for the level $3p^3P_{J=2}$ as a function of pressure and current can be seen in figure 6. The level $3p^3P_{J=1}$ gave the same decay rate values and variation with pressure and current within an average difference of $\pm$ 0.0022 ns^{-1} ($\sim$4.5%).

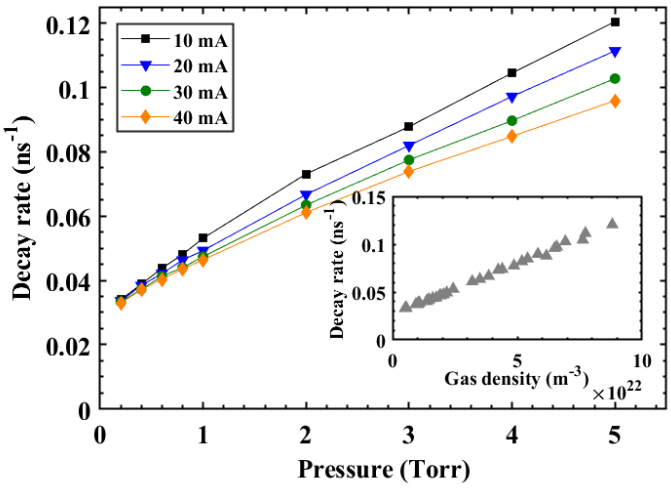

Figure 6: Variation of the effective decay rate of the $3p^3P_{J=2}$ state with pressure and current. In the inner figure, the same decay rates are plotted *versus* total gas density.

As expected, we see an increase of the decay rate with pressure. We also see a small decrease with increased current, which can be explained by the decrease in gas density due to a temperature increase. The inner figure shows the same data but plotted as function of the total gas density. The clear linear dependence shows that it is reasonable to assume that the decay rate depends only on the total gas density and is insensitive to the gas composition (in our experimental conditions). Therefore, $\sum_Q k_Q[n_Q] \rightarrow k_Q[N]$, with N being the total gas density. The natural lifetime is obtained from the inverse of the intercept at zero pressure of a linear fit to this data. The value found is around τ_0 = 37.3 ns, which is close to experimental values found in literature, 34.7 $\pm$ 1.7 ns in [75] and 35.1 $\pm$ 3.0 ns in [93], but slightly higher than the theoretically calculated value given by the NIST (31.1 ns).

The O atom densities were calculated from the TALIF signal using our experimental values for the natural lifetime and the measured decay rates for each plasma condition (*i.e.* a_O in equation (6) is equal to $A(=1/\tau_0)/A^*$). For the actinometry calculation the quenching rates for the two oxygen lines, O777 and O845, are required. Due to the lack of data in CO_2, we used the quenching rate coefficients available for pure O_2 plasma. The fact that the gas density is the main parameter in the quenching process gives us confidence in that the error induced is insignificant for the final result. Nevertheless, we determined experimentally how the quenching coefficient for the O845 line (from $O(3p^3P)$), changes with gas composition, from pure O_2 plasma to pure CO_2 plasma in our experimental conditions.

The average value for k_Q obtained in pure O_2 is $k_Q^O = 9.35 \times 10^{-16}\ m^3 s^{-1}$, very close to the value taken from literature. The addition of CO_2 has only a small effect, between 2 and 10%, and the average value is $k_Q^O = 9.59 \times 10^{-16} m^3 s^{-1}$. Therefore, we make the same assumption for both oxygen emission lines used for actinometry, and assume that the quenching coefficients for O_2 plasma are also valid for CO_2 plasma, with a maximum error around 10%. *A posteriori* analysis showed that varying all these quenching coefficients by 10% causes a change of less than 1.5% in the absolute O atom values obtained by actinometry.

5 CO_2 dissociation and O atom densities

5.1 Dissociation fraction in continuous CO_2 plasma

The dissociation fraction of CO_2 can be determined from the measurement of the CO density by means of *in situ* FTIR absorption. These measurements were performed with the short discharge tube (23 cm), which fits into the sample compartment of the FTIR; however, the atomic oxygen measurements were made in the long discharge reactor (67 cm). The *radii* of both tubes are the same, and there is no axial gradient along the tube since the diffusion dominates over the motion due to the gas flow, homogenizing the concentrations as has been confirmed by Raman scattering measurement along the tube axis [57].

Therefore, the main difference between the two discharge tubes is the length between the electrodes, which, for a given flow, implies a different residence time (τ_{res}) of the gas in the plasma. In order to estimate the CO produced in the long tube, the dependence of the CO density on the residence time was measured *in situ* in the short tube by varying the gas flow for the different plasma conditions. Additional downstream measurements using both long and short tubes confirmed that the CO_2 dissociation fraction is the same in both reactors for a given residence time.

Figure 7 shows the measured variation of the absolute CO density and the CO fraction, normalized over total gas density N, for different currents and pressures in the long discharge tube. The absolute CO density increases monotonically with pressure, whereas the CO fraction over total gas density first increases slightly with pressure up to 1 Torr, and then becomes almost constant at higher pressures. Both graphs show a saturation at higher currents. It is worth noting that during these measurements the CO_2 densities were also measured and that the carbon balance was always fulfilled for all pressures and currents. Therefore the CO densities presented in figure 7 give an upper limit to the O atom densities that can be expected in the gas mixture. The FTIR *in situ* measurements also provide information about the vibrational excitation of CO and CO_2 that will be correlated with the O atom density in a future work.

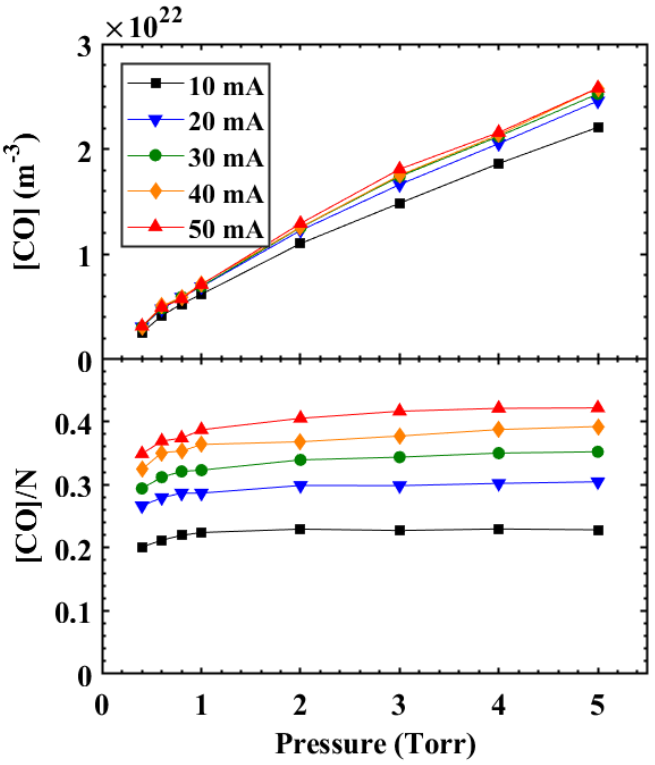

Figure 7: Variation of the CO density (top graph) and CO fraction (bottom) as a function of pressure for different currents.

5.2 Absolute O atom densities

The atomic oxygen densities determined by both actinometry and HR-TALIF are shown in figure 8 as a function of pressure and current. The graph to the left (a)) shows the absolute O atom density and figure b) (on the right) presents the O atom fraction, (absolute O atom density divided by the total gas density). The TALIF data in these graphs were obtained with the absolute calibration based on the TALIF fluorescence method (see section 3.2.2) and using $\sigma^{(2)}_{Xe}/\sigma^{(2)}_{O} = 1.9$ from [75]. Figure c) (inner figure of b)) will be discussed bellow. Three main observations can be made:

- Both O atom emission lines used for actinometry give very similar values.
- The trend of O atom absolute density variation as a function of pressure obtained with both HR-TALIF and actinometry is the same. It shows an increase in density below 1-2 Torr and then a saturation, which results in a clear decrease in the O atom fraction, O/N, above 1 Torr.
- The densities obtained with actinometry are systematically lower than with TALIF.

Let us first discuss the accuracy of the absolute values obtained with actinometry. The CO fractions shown in the previous section were used as input for the Boltzmann solver in order to obtain the EEDF and the excitation rate coefficients, required to obtained the O atom densities, as detailed in section 3.1.2. These CO densities, although determined with a line-of-sight integrated technique, correspond to the correct values necessary to process the O emission data because of the spatial homogeneity in the CO densities (discussed in section 5.1).

The fact that both O777 and O844 give similar densities suggests that processes populating the detected excited states other than direct electron impact excitation of atoms are not significant in our plasma conditions [94] (*i.e.* two-step excitation via metastable states or cascading from higher excited levels can be neglected). When looking more closely, the line O777 gives slightly higher O atom densities in the low pressure range. In the case of a pure O_2 plasma, it is commonly considered that the line O777 is less reliable because it can have a stronger contribution from dissociative excitation of ground state or metastable O_2 molecules [94]. The dissociative excitation of ground state O_2 was accounted for in our calculations; however its contribution is very small due to the low O_2 fraction in a CO_2 plasma [50] and the higher energy threshold for this process. Similarly, the dissociation excitation from metastable states of O_2 is expected to be very low. Dissociative excitation from CO_2 could however occur, but it was not included in our calculations due to lack of cross-section data for this process.

In spite of the consistency between the results obtained with the two oxygen emission lines, the absolute densities measured can still be sensitive, for instance, to the electron impact excitation cross sections used in the calculations, as discussed in [65]. In addition, the cross section set used to calculate the electron distribution function (EEDF) may also affect the estimated densities. As an example, when calculating the O atom densities with a different set of cross sections (Morgan + Phelps) for a similar gas composition, the O atom densities obtained are about 20% higher than with the IST set. Therefore, the disagreement between TALIF and actinometry could be partially explained by inaccuracies in the cross sections used. However, preliminary measurements by cavity ring down spectroscopy (CRDS) in the same experimental conditions show good agreement with the actinometry densities [95] while on the other hand, the densities obtained from TALIF measurements could also be overestimated.

In figure 8 a) and b) the solid lines represent the TALIF data obtained with the absolute calibration based on the TALIF fluorescence and using $\sigma^{(2)}_{Xe}/\sigma^{(2)}_{O} = 1.9$ [75]. Figure 8 c) (inner figure of b)), shows the data only for 40 mA, for readability, obtained with the two methods (TALIF fluorescence and TALIF profile), in good agreement. It also includes the actinometry data for both lines. Both TALIF curves give densities markedly higher than actinometry. These absolute O atom densities determined with TALIF are directly proportional to the ratio of the two-photon absorption cross section of xenon *versus* oxygen, determined by titration [75]. Recent preliminary measurements obtained by direct laser absorption [83] indicate that the value of the Xe cross section may be significantly lower than the previously reported value, roughly half of the previous value (for oxygen the two-photon absorption cross section is known [81]). This would tend to decrease the results obtained with TALIF. In figure 8 c) the O atoms fractions determined by TALIF but using this new cross section value are also plotted, showing very good agreement with actinometry. The new value of the Xe two-photon absorption cross section is to be confirmed. In any case, this cross section is the biggest source of uncertainty in TALIF measurements. Additionally, small deviations of the laser beam spatial distribution from the assumed Gaussian profile can affect significantly the final O atom density results because of the square dependence of the TALIF signal with the beam waist.

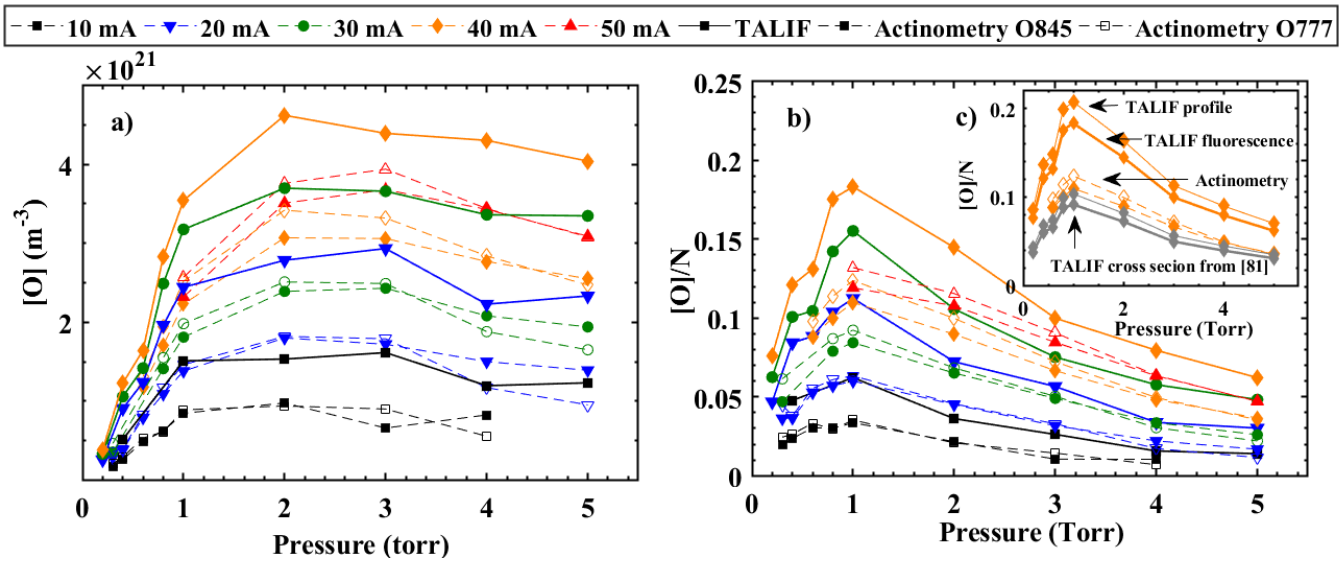

Figure 8: Variation of the absolute O atom density (left, a)) and the O atom fraction normalized to the total gas density (right, b)) with pressure for different currents measured with both TALIF and actinometry. N is the total gas density, calculated using T_{gas} measured with TALIF for TALIF O_{atom} densities and with T_{gas} measured by FTIR for actinometry O_{atom} densities. The TALIF data in these graphs correspond to the absolute calibration based on the TALIF fluorescence and using $\sigma^{(2)}_{Xe}/\sigma^{(2)}_{O} = 1.9$ [75]. Figure c) (inner figure of b)) shows a comparison of the data only for 40 mA between actinometry and both TALIF profile and TALIF fluorescence for the mentioned cross section and with the preliminary direct measurement from [83].

Therefore, despite the good agreement between the two techniques in the trends, the absolute values can still have significant uncertainties due to their sensitivity to the parameters detailed above, and an error not lower than 30% is estimated. Even taking this into account, O atoms represent a large proportion of the total gas mixture in our conditions. The maximum of $[O]/N \sim$ at 1 Torr, shown in figure 8 b) is 0.18 for TALIF fluorescence (0.21 mA for TALIF profile) and 0.12 for actinometry. The ratio $[O]/CO$ reaches a maximum value close to 40% for 1 Torr 50 mA, meaning that for some conditions almost half of the oxygen resulting from CO_2 dissociation remains in the form of free O atoms and do not recombine into oxygen molecules.

Beyond the uncertainties concerning the O atom absolute densities, the consistency of the trends shown in figure 8 for both actinometry and TALIF when the current and pressure are varied is remarkable. The atomic oxygen density continuously increases with current over the range measured, not showing the same saturation seen for CO (see figure 7). The O atom density increases with pressure up to around 2 Torr and then further reaches a "plateau", showing only a slight decrease with increasing pressure. This trend indicates that there is a change of regime around 1-2 Torr which is even more evident in O atom fraction (right graph in figure 8). $[O]/N$ increases up to 1 Torr, passes through a maximum and then decreases rapidly. Therefore, two distinct regimes are observed with a transition between 1 and 2 Torr, which could be caused either by a change in the production of O atoms or due to a change in their loss processes.

The variation of the CO and O atom fraction with pressure shown in figures 7 and 8, is noticeably different. Both CO and O densities show an increase below 1 Torr, but for higher pressures $[CO]/N$ becomes almost constant, while $[O]/N$ decreases markedly. Since the creation rate of both O and CO from CO_2 dissociation should be similar (assuming a negligible contribution to $[O_{atom}]$ from the dissociation of CO), the loss rate of O atoms must increase faster than for CO with increasing pressure. This possibility will be examined in the following section.

5.3 O atom loss frequency

To get insight into the loss mechanisms, the lifetime of the O atoms in the plasma was measured. In a glow discharge at a few Torr, it is expected that the recombination of oxygen atoms at the walls will be the major loss process although gas phase losses must also be considered (see section 6.2.1). While many works have reported the recombination probability of atomic oxygen (γ_O) in pure O_2 plasmas, very few values are given in CO_2 plasmas. The recombination probability on silica or Pyrex has been

studied in O_2 plasma especially for atomic sources and thermal shields for spacecraft re-entry [96, 97] but even for O_2, the reported values of γ_O are largely scattered for a given material surface. Apart from the uncertainties inherent in certain measurement methods (e.g. titration with NO), among the main reasons for these differences are the pre-treatment history of the surface and the wall (surface) temperature. Another source of discrepancies between the γ_O values obtained comes from the plasma exposure conditions of the surface. Values of γ_O on Pyrex and/or quartz surfaces have been measured in O_2 plasma either in *spatial post-discharge* by measuring a longitudinal profile of O atoms density downstream the plasma [51,98,99] sometimes at elevated surface temperature [100,101], or in *temporal post-discharge* by monitoring the decay of O atoms density after switching off the plasma [52, 102–105], or in *stationary discharge* by measuring a spatial gradient of O atoms above the surface studied [106–109]. Values of γ_O obtained in *spatial post-discharge* are often at least an order of magnitude lower than values obtained with the surface under direct plasma exposure. The reasons for this effect are still uncertain. At pressures below 1 Torr in O_2 it has been claimed in [59] that ion bombardment can clean active sites and increases the chemical activity of the surface. In CO_2 plasma the values of γ_O are much more scarce [26, 40, 50] and obtained in conditions difficult to compare with the values obtained in pure O_2.

In order to obtain reliable data on the role of oxygen atoms on the kinetics of a CO_2 plasma it is important to be able to determine the loss frequencies of oxygen atoms while keeping the reactor surface directly exposed to CO_2 plasma. In order to determine the lifetime of the O atoms under plasma exposure we have used a similar method to that used by Lopaev and Smirnov [58, 59] which is based on a partial modulation of the discharge current (square modulation, with a current variation around 15%, depending on the plasma conditions). In this way, the gas composition and the flux of various species (atoms, ions) towards the surface is only slightly modulated during the cycle. In addition, as the surface temperature is known to change the recombination probability at the wall, the surface temperature is kept constant at 323K (50^0C). Given that TALIF and actinometry provide consistent trends, these measurements can be made simply by recording the variation of the actinometry signal over time. The modulation period was fixed at 146 ms, long enough to fit the decay time for all conditions.

The measurements of the current and the optical emission intensities for argon and both oxygen lines are shown in figure 9, as an illustrative example, for 2 Torr 50 mA. Clearly, the Ar line follows the same trend as the current, while both atomic O lines show an exponential increase or decay as the current is modulated. The figure in the bottom shows the ratio between the O lines and the Ar line, with a single exponential fit [50, 104]. A single exponential curve fits very well the experimental data, which was the case for all pressures studied. The error in the exponential fit of this decay (residual of the fit), is very small and on average around 0.5%. The single exponential behaviour suggests that the loss mechanism is controlled by a first order process, which will be discussed in section 6.2. A second order mechanism would lead to an hyperbolic decay $\sim 1/t$, but this type of fitting was not following the data as well as the exponential fit, giving a residual value 36% higher.

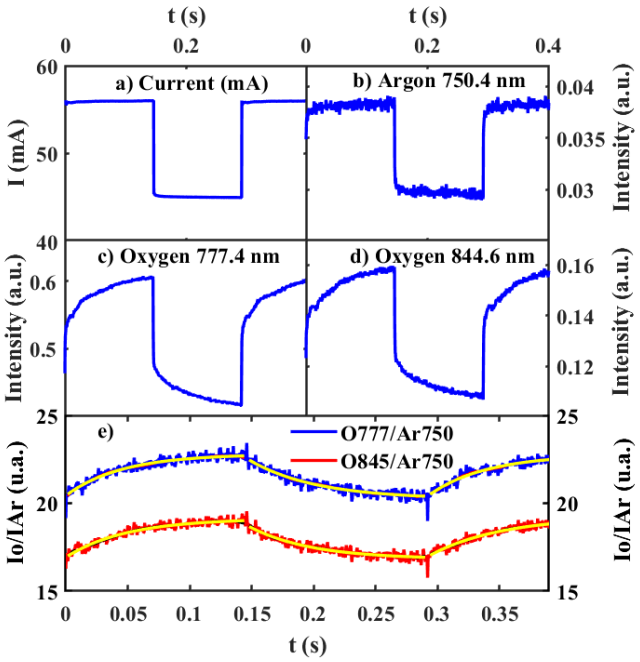

Figure 9: Temporal variation of: a) Current flowing in the discharge; b) Intensity of the Ar750 nm line; c) Intensity of the O777 nm line; d) Intensity of the O845 nm line and e) Ratios I_O/I_{Ar} for both O lines and the corresponding exponential fit.

From equation (4), we can assume that the temporal variation of the O atom fraction $[O]/N$, is well represented by the temporal variation of the emission line intensity ratios I_O/I_{Ar}. This supposes that both the reduced electric field and the gas temperature do not change significantly during modulation, or that they change so fast as to not influence the O atom kinetic measurement. In the case of the electric field, the highest variation during modulation happens for 5 Torr 50 mA, reaching around 4% for a change of 21% of the current. Additionally the time

variation of the electric field is relatively fast, around 10 μs. Concerning the gas temperature (which affects E/N though its influence in the gas density), in the worst case the induced variation on the total gas density is around 7% with a characteristic time lower than 5 ms [53], considerably faster than the O atom lifetime. Consequently, the O atom loss frequency ν_O^{loss} can be obtained directly from the time variation of the ratio of the intensities.

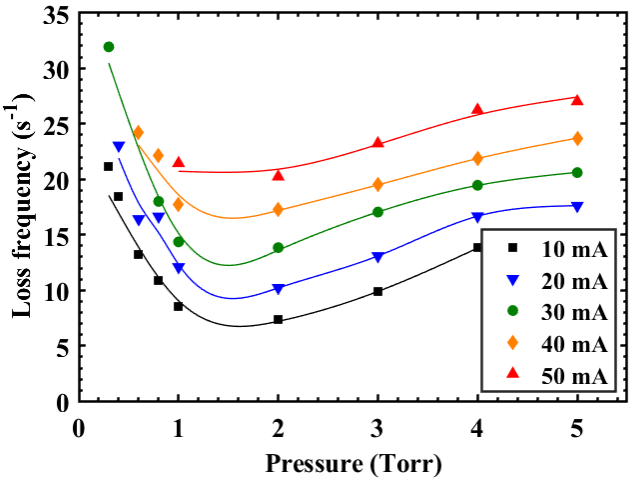

Figure 10: Variation of the loss frequency, ν_O^{loss}, with pressure and current.

The loss frequencies, obtained from the average of the values for the two atomic oxygen lines, are plotted for different currents and pressures in figure 10. The error in the loss frequency is more related to the reproducibility and the small differences between the exponential increase and decay than to the error in the exponential fitting; the estimated error is of the order of 15%. The obtained ν_O^{loss} values fall mostly between 10 and 25 s^{-1} and we can again clearly differentiate two regions. The loss frequency first decreases with pressure, passes through a minimum around 1-2 Torr and then increases slowly with pressure above 2 Torr. This correlates very well with the pressure trend in the O atom density. The loss frequency increases markedly with current at all pressures. This change of regime, the strong increase of the O atom loss frequency at low pressure and the corresponding variation of the O atom density is similar to that observed in pure oxygen plasma with a similar discharge in [59]. However loss frequencies up to ~2 times higher were measured in the case of O_2 plasma compared to CO_2 plasma. Therefore CO and CO_2 molecules appear to influence the loss mechanisms of O atoms as it will be discussed in the following section.

6 Discussion

The O atom densities, measured *in situ* in a glow discharge tube of 1 cm radius, show two regimes when varying the pressure: the O atom fraction increases with pressure below 1 Torr, passes through a maximum and then decreases for higher pressures. The corresponding O atom loss frequencies measured under plasma exposure show the opposite behaviour, decreasing with pressure up to 1 Torr and subsequently increasing for higher pressures. Both are strongly correlated. The CO trend at low pressure is similar but differs form the O atom at higher pressures. One might expect the dissociation fraction of CO_2 to depend mostly on the energy density dissipated in the plasma. Therefore figure 11 summarizes all the O atom and CO data, plotted as a function of the energy density (*i.e.* specific energy input, SEI).

6.1 CO and O atom densities

For all currents the O atom density and the O atom fraction pass through a maximum as a function of the SEI, a maximum which is broader for higher currents and which increases linearly with the energy density. A similar trend was observed by Vesel *et al.* [37] in the spatial post-discharge of a microwave plasma ignited in a 0.25 cm radius quartz tube. As a function of pressure, while a maximum was observed at 1 Torr for all discharge currents in our experiments, Vesel *et al.* shows a maximum in the relative O atom density around 20 Pa (0.15 Torr) for all microwave powers.

The fact that the maximum of O atom density occurs at higher SEI for higher current can be simply explained by the increase in the electron density, leading to an increase of the dissociation rate. The subsequent decrease when increasing pressure is claimed by Vesel *et al.* [37] to be due to a decrease in the production rate (related to a decrease of the electron temperature caused by the lower mean free path), along with an increase of the gas phase recombination processes. The bottom graph of figure 11 shows that the minimum of the O atom loss frequency also increases linearly with the SEI, similarly to the maximum of the O atom density. This suggests that the maximum in O atom density is more related with a change in the loss processes rather than a change in the kinetics of the creation processes when the pressure is increased.

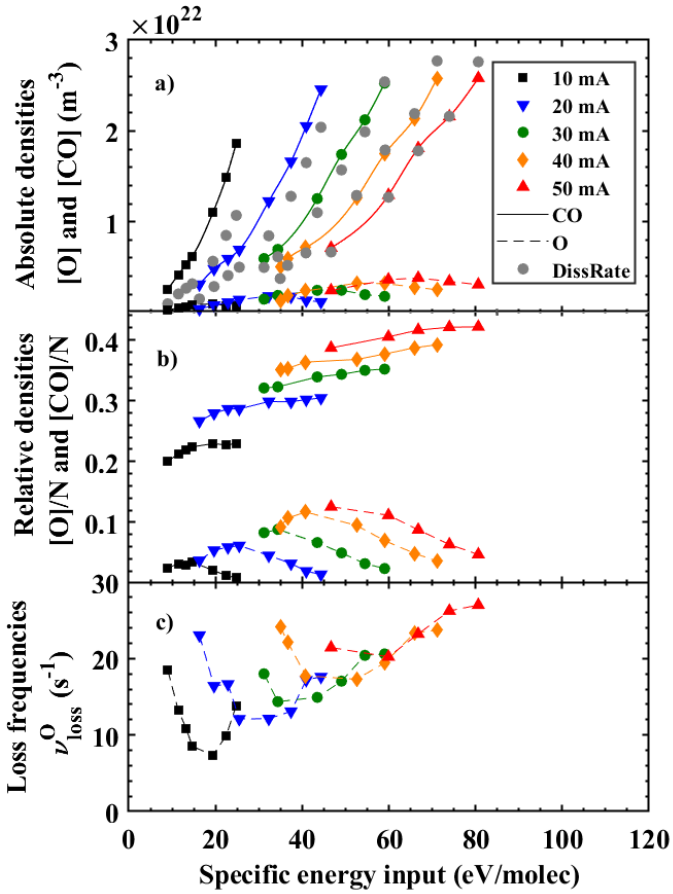

Figure 11: a) Variation of the absolute densities and b) fractions of CO and O atom (average of actinometry lines in figure 8) along with the calculated dissociation fraction (using Polak's cross section [110]) and c) the corresponding O atom loss frequencies as a function of the specific energy input.

The similar trends in the O atom density for the two different types of discharges are noteworthy and could be related to similarities in the surface of the reactors (quartz and Pyrex). The different pressure at which the maximum of $[O]/N$ occurs (1 Torr here and 0.15 Torr in the case of Vesel *et al.*) could be due to the different geometry (different radius, 1 cm *versus* 0.25 cm) of the reactor, which may affect both the electric field and the loss processes, impacting the O atom densities obtained [65]. Other possible differences are the higher ion flux in microwave plasmas compared to DC [102], slightly different surface composition (quartz versus Pyrex), different surface and/or gas temperature or the usual differences in the O atom loss frequencies in a spatial post-discharge *versus* in steady state plasma (as discussed in section 5.3 and [50, 102, 111]).

The CO density is equal to the maximum density of O atoms that either remain as free atoms or that recombine into molecular oxygen. This may be different to the total amount of O atoms produced, since the recombination of CO with O is possible and cannot be excluded, but this would not be detected from the measurements of CO. It is clear that the O atoms are more affected by loss processes than CO over the whole range of pressures and currents studied, otherwise their densities (and trends with pressure and current) should be similar. The atomic oxygen density represents between 10 to 40% of the CO, and is therefore always a significant part of the gas mixture in our conditions. At low SEI, the quantity of O atoms produced is low, and almost all are recombined, most likely into O_2 (O_3 can be considered to be a minor specie in our pressure range [112]). However at around 50 eV/molecule the O atom density reaches values above 35% of the density of CO (according to actinometry). For all currents, the O atom fraction first increases linearly with SEI, in spite of the high loss frequency observed for these conditions. In contrast, at higher SEI, the O atom fraction decreases linearly. The loss mechanisms of O atoms are therefore more efficient at high SEI, which will be discussed more in detail in section 6.2.

Contrary to the case of O atoms, the CO density increases with the energy input, although tends to saturate at high current and SEI. This is expected since the more we dissociate, the more probable are collisions between electrons and other molecules instead of CO_2. The increase of CO with energy input can be mostly explained by direct electron impact dissociation. The rate for this process is also included on the top graph of figure 11 for comparison. This dissociation rate was calculated with the expression:

$$R = n_{e-} \cdot K_{diss} \cdot [CO_2] \cdot \tau_{res} \quad (9)$$

where n_{e-} is the electron density calculated from the measured current and the drift velocity (calculated from fitting the data from [113]), K_{diss} is the dissociation rate coefficient from Polak and Slovetsky [110], $[CO_2]$ are the measured CO_2 densities and τ_{res} is the residence time. It is beyond the scope of this paper to discuss the electron impact dissociation cross section, and a detailed critical analysis of discrepancies in the cross sections from different sources is given by Grofulović *et al.* [114]. The use of Polak's cross section here follows the recommendation in [114] and is only to illustrate that the CO trends follow what would be expected from electron impact dissociation. An investigation dedicated to establish the value of the electron impact dissociation rate coefficient will be presented in another publication [115]. Nevertheless, the results in figure 11 suggest the validity of the rate coef-

ficients calculated from the cross section from Polak and Slovetsky [110].

6.2 O atom loss processes

The measured loss frequencies can be the result of both surface loss processes and/or due to gas phase reactions:

$$\nu_{loss}^{O} = L_{gp} + \frac{\gamma_O \cdot \upsilon_{th}}{2R} \tag{10}$$

where L_{gp} represents the contribution of the gas phase losses, γ_O is the O atom surface loss probability, υ_{th} is the thermal velocity of the O atoms and R is the radius of the discharge tube. In principle, ν_{loss}^{O} can have a very complex dependence with different plasma parameters including gas temperature [59], wall temperature [104], flux of O atoms, etc. as discussed in detail by Guerra [116]. Figure 11 shows that for higher pressures (above 1 Torr) the O atom loss frequency increases linearly with the energy input. This dependence is in fact related to the linear increase of the gas temperature with the SEI (shown in figure 4 b)), which is clearly observed in figure 12, showing the measured loss frequencies plotted as a function of T_{gas}. For higher pressures, from 2 to 5 Torr, we see a direct correlation of the loss frequency with the gas temperature, which increases with pressure and current as shown in figure 4 a). We checked the dependence of the measured loss frequencies with many other variables, such as the O atom density, the electron density, etc. However, no obvious correlation with any other variable except the gas temperature was found. Therefore we conclude that in our conditions the gas temperature plays a dominant role in the recombination process and the effect of other possible variables is less relevant. It is worth remembering here that the wall temperature is thermalized to 323 K for all the experiments and therefore the trend shown in figure 12 is not the result of surface heating.

The gas temperature can affect the recombination processes in two possible ways: either by an increase in the gas phase recombination processes, whose rates are temperature dependent, or due to an increase of the kinetic energy of the O atoms reaching the reactor walls, and therefore with higher energy to overcome an activation energy for recombination with adsorbed species at the wall (*e.g.* O_{ad} or CO_{ad}), as proposed in the case of pure O_2 discharges by Booth *et al.* [59]. Both possibilities are discussed in the following sections.

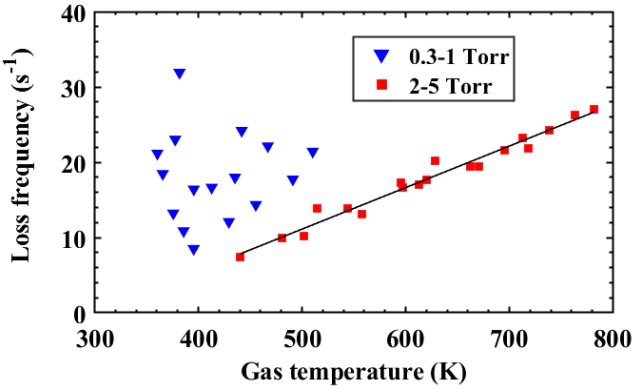

Figure 12: Loss frequency plotted as a function of the gas temperature. In blue triangles, the data for pressure from 0.3 to 1 Torr, included, and in red squares the data from 2 Torr up to 5 Torr. A linear fit for the data at higher pressures is also included.

6.2.1 Gas phase recombination

There are several gas phase reactions reported in the literature [33, 41, 42, 44, 117, 118] that can remove atomic oxygen from the gas mixture. Only a selection of them is listed in table 1, and the corresponding reaction rates obtained for the most relevant reactions (underlined in the table, and discussed bellow) are plotted in figure 13, along with the measured loss frequencies. Note that reactions 10 and 11 correspond to a gas-phase effective way of describing reactions at the surface (wall). They are further discussed at the end of this section.

- **O+O and O+CO (+M)**. Comparing both reactions and their variation with gas temperature, the recombination of O atoms into oxygen molecules is more efficient than the reaction with CO giving back CO_2. This is consistent with Sepka *et al.* [39], where a mixture of CO and O atoms in the post-discharge of an O_2 plasma showed that the presence of CO in gas phase did not affect the O recombination processes and that the CO concentration in gas phase was not significantly altered by the presence of oxygen atoms. However, the rates for these reactions are strongly temperature dependent. Indeed, the rate of the recombination reaction between oxygen atoms increases by one order of magnitude over the range of gas temperatures studied, while the rate of recombination with CO increases by about two orders of magnitude. Consequently, at the highest temperatures, which correspond to the highest pressures, the rates for both processes tend to converge reaching the same order of magnitude.

Table 1: Main reactions involving oxygen atoms in CO_2 plasmas found in literature. For the gas phase reactions the units are $cm^3\ s^{-1}$ or $cm^6\ s^{-1}$ for two or three body reactions respectively. For gas/surface reactions the units are specified. The number of the reactions corresponding to the rates plotted in figure 13 are underlined.

Type	Reaction R	N^{er}	Rate coefficients	Reference
Gas phase	$O+O+M \rightarrow O_2+M$	1	$5.2\cdot10^{-34}\cdot exp(^{900}/_{T_{gas}})$	[41]
Gas phase	$O+CO+M \rightarrow CO_2+M$	2	$8.2\cdot10^{-34}\cdot exp(^{-1510}/_{T_{gas}})$ $M=CO/O_2$	[41]
		3	$1.6\cdot10^{-33}\cdot exp(^{-1510}/_{T_{gas}})$ $M=CO_2$	[41]
Gas phase	$O+CO \rightarrow CO_2+h\nu$	4	$4.15\cdot10^{-18}\cdot exp(^{-1600}/_{T_{gas}})$	[117]
Gas phase	$O+CO_2 \rightarrow CO+O_2$	5	$2.8\cdot10^{-11}\cdot exp(^{-26500}/_{T_{gas}})$	[33, 117]
Gas phase	$O+O_2+M \rightarrow O_3+M$	6	$5.5\cdot10^{-31}\cdot T_{gas}^{-1.2}$ $M=O_2$	[41]
		7	$5.5\cdot10^{-31}\cdot T_{gas}^{-1.2}$ $M=CO$	[41]
		8	$1.7\cdot10^{-30}\cdot T_{gas}^{-1.2}$ $M=CO_2$	[41]
Gas phase	$O+O_3 \rightarrow 2O_2$	9	$3.1\cdot10^{-14}\cdot T_{gas}^{0.75}\cdot exp(^{-1575}/_{T_{gas}})$	[41]
Gas / surface	$O+CO+wall \rightarrow CO_2+wall$	10	$^{7.4\cdot10^{-17}}/_{R}$ $cm^3\ s^{-1}$ *	[41, 118]
Gas / surface	$O+O+wall \rightarrow O_2+wall$	11	$^{5\cdot10^{16}}/_{[CO]}$ $cm\ s^{-1}$ **	[41, 44, 118]

* R is the radius of the reactor in cm. **[CO] in $cm\ s^{-3}$. The effective rate constant for this reaction is calculated with equation 11.

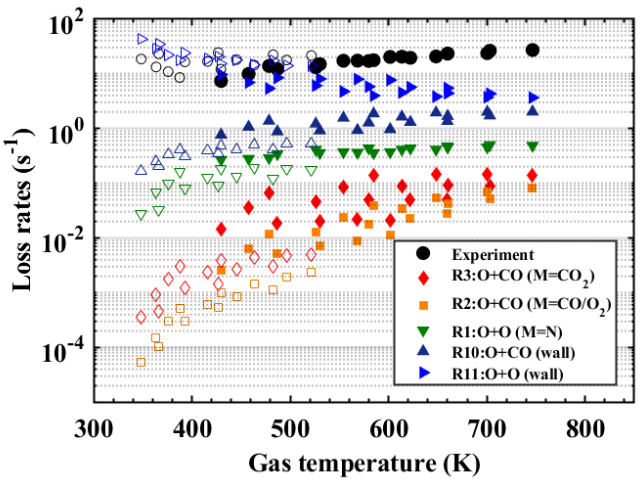

Figure 13: The experimentally observed loss frequencies ν^O_{loss} plotted versus T_{gas} along with the calculated rates for different reactions summarized in table 1. The empty symbols are for data between 0.3 and 1 Torr and the full symbols are for data between 2 and 5 Torr.

- **Vibrationally excited molecules**. The reaction between O and CO could be enhanced by the vibrational excitation of CO, which has been measured under similar plasma conditions [54]. No rates are available in the literature, to our knowledge, for the reaction of O with vibrationally excited CO. A reaction between atomic oxygen and vibrationally excited CO_2, producing CO and O_2, is also possible. The rate for this reaction, as presented in table 1, is rather low, however it is expected to increase with the vibrational excitation of CO_2 [33] and could contribute to the different behaviour of O atom and CO as a function of the energy density. Nevertheless, in a glow discharge the CO_2 dissociation is believed to be mostly due to electron impact and, at the same time, the vibrational excitation of CO_2 is known to decrease with increasing pressure [54]. Additionally, the higher the vibrational excitation, the lower the density of vibrationally excited particles, as can be deduced from the vibrational distribution function [33].

- **Ozone formation and oxidation**. The reaction between atomic oxygen and molecular oxygen to create ozone (reactions 6-8 in in table 1), has a rate constant between those of reactions 1 (O+O) and 3 (O+CO), plotted in figure 13. This reaction could be followed by further reaction of the created ozone with O atoms (creating two O_2 molecules), consuming an extra O atom (reaction 9). However the density of the reactants (O_3 and O) is relatively low and therefore this reaction may contribute but will not play an important role in the overall O atom loss

rate.

- **C atom oxidation reactions**. The carbon balance was checked by means of FTIR, and was found to be basically fulfilled with the measured amounts of CO and CO_2. Therefore reactions with C atoms are not expected to have a significant impact on the overall O atom balance. If some carbon is created by dissociation of CO, it will be subsequently oxidized rapidly back to CO.

In spite of the increase of the rates of the above-mentioned gas phase recombination reactions with the gas temperature, the rates are still at least one order of magnitude lower than the observed loss rates. The potential contribution of reactions of O with vibrationally excited CO, or CO_2, cannot be excluded, and potentially can have reaction rates that are higher than for vibrational ground state molecules, but it is not probable that this type of reactions can increase the gas phase reaction rates enough to reach the experimental loss frequencies.

Reactions at the wall. Reactions 10 and 11 in table 1, plotted in figure 13, account for the recombination of gaseous oxygen atoms with either oxygen atoms or with CO at the walls [41]. They represent therefore surface processes, without specifying their nature, since they come from fitting of experimental data [118], and are valid for the conditions of those experiments (1-2 Torr, T_{wall}=300-390K and between 1 and 10 mA cm^2). The loss rates corresponding to reaction 10 can be calculated by multiplying directly by the measured [CO]. In the case of reaction 11, the corresponding effective rate constant in s^{-1} is calculated by the expression [44]:

$$k_{eff} = \frac{k \cdot S/V \cdot K_{diff}}{k \cdot S/V + K_{diff}} \tag{11}$$

where k_{eff} is the effective rate constant, plotted in figure 13, k is the rate coefficient in table 1, S is the surface area in contact with the plasma, V is the volume of the plasma and K_{diff} is the diffusion rate towards the wall $= 1/\tau_{diff}$, which will be defined bellow. The loss rate values obtained with these expressions are higher than the rates previously discussed, and are much closer to the experimental values, especially for the reaction $O+O+wall \rightarrow O_2$, and particularly in the range between 1 and 2 torr (400-600K). This suggest that surface recombination dominates over gas phase reactions of O atoms under our experimental conditions.

6.2.2 Surface recombination

The loss rate due to recombination at the reactor walls can be expressed as [119]:

$$\tau = \frac{1}{K_{wall}} = \tau_{diff} + \tau_{loss} = \frac{\Lambda_O^2}{D} + \frac{V}{S}\frac{2(2-\gamma)}{\upsilon_{th}\gamma} \tag{12}$$

where γ is the wall loss probability (of the O atoms in this case), V and S have already been defined for equation (11), υ_{th} is the thermal velocity of the O atoms given by the expression $\upsilon_{th} = \sqrt{8k_BT/\pi \cdot m_o}$, where m_o is the mass of the oxygen atoms ($m_o = 2.66 \times 10^{-26}$ kg) and D is the diffusion coefficient of atomic oxygen. Λ_O is the diffusion length given, for a cylindrical reactor by:

$$\frac{1}{\Lambda_O^2} = \left(\frac{\pi}{L}\right)^2 + \left(\frac{2.405}{R}\right)^2 \tag{13}$$

where L is the length and R is the radius of the cylindrical reactor, in our case $\Lambda_O = 0.42$ cm. Two expressions have been found in literature to calculate the diffusion coefficient of O atoms in CO_2. From Cenian *et al*. [41]:

$$D = D(0) \cdot P^{-1} \cdot (T/273)^{3/2} \tag{14}$$

where $D(0) = 190$ $cm^2 s^{-1}$ is the diffusion coefficient at 1 Torr and 273 K, P is the pressure in Torr and T is the gas temperature. Or, otherwise [54]:

$$D = \frac{1}{3} l \upsilon_{th} = \frac{1}{3}\left(\frac{k_BT}{\sqrt{2} \cdot P\pi d^2}\right) \cdot \sqrt{\frac{8k_BT}{\pi \cdot m_o}} \tag{15}$$

where l is the mean free path, d is the kinetic diameter of the oxygen atom (assumed to be similar to the molecular oxygen, 346 pm [120]) and υ_{th} is the thermal velocity of the oxygen atoms. According to these equations, the maximum of τ_{diff} is for 5 Torr 10 mA, and ranges between 1.8 ms (equation (14)) and 3.2 ms (equation (15)). As the minimum lifetime (τ_{loss}) in our conditions is close to 20 ms we can assume that $\tau = \tau_{diff} + \tau_{loss} \approx \tau_{loss}$ ($\tau_{diff} \ll \tau_{loss}$). Taking this into account in equation (12) we can calculate the loss probability with the expression:

$$\gamma_O = \frac{2R \cdot \nu_{loss}^O}{\upsilon_{th}} = \frac{2R}{\tau_{wall}\upsilon_{th}} \tag{16}$$

which is equivalent to equation (10) but already discarding the contribution of gas phase losses. In this equation the value of temperature used for the thermal velocity should represent the temperature of the atoms reaching the wall. This temperature, $T_{near\ wall}$, is lower than T_{gas} discussed in section 4.1 because of the radial temperature profile in the tube. The low value of the mean free

path (the maximum value is 0.25 mm) means that the O atoms will be thermalized to this lower temperature before reaching the wall [59]. Measurements of $T_{near\ wall}$ made with TALIF for all pressures at 40 mA, ranging from 375 at 1 Torr to 500K at 5 Torr, allow us to estimate this temperature. In figure 14 the obtained loss probabilities using both T_{gas}, for comparison, and $T_{near\ wall}$, are plotted *versus* 1000/T being T=T_{gas} or T=$T_{near\ wall}$ respectively. Loss probabilities obtained for O_2 plasma under the same experimental conditions and the same experimental setup are included as well for comparison (data extracted from [59]).

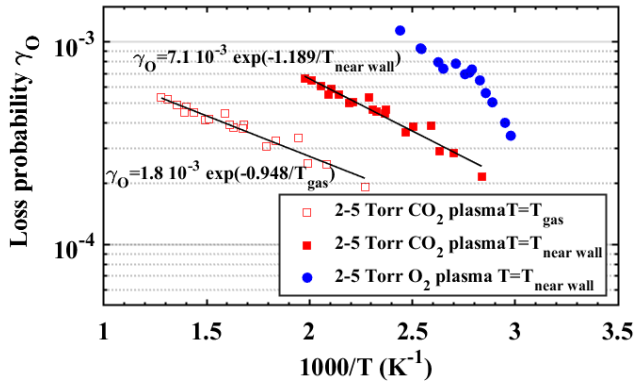

Figure 14: Loss probabilities γ_O plotted versus $^{1000}/_{T}$, calculated and plotted using T=T_{gas} and T=$T_{near\ wall}$ for CO_2 plasma with the corresponding exponential fittings, and for O_2 plasma *versus* T=$T_{near\ wall}$ (data extracted from [59]).

In both CO_2 and O_2 we observe a clear dependence of γ_O on the gas temperature. In the case of CO_2 plasmas the obtained loss probabilities are in the range of 2-6 $\times$ 10^{-4} and clearly follow an exponential trend, *i.e.* an Arrhenius dependence, which can be described by [116]:

$$\gamma_O = A \cdot exp\left(-\frac{E_{act}}{k_B T_{near\ wall}}\right) \qquad (17)$$

The activation energy, E_{act}, obtained from this expression considering $T_{near\ wall}$ is 0.103 eV (compared to ~0.13 eV for pure oxygen [59]). This dependence with gas phase temperature, and not only with surface temperature, has been recently observed for the first time in pure O_2 [59]. It is expected from a first order process, an Eley-Rideal surface recombination mechanism, where an adsorbed atom or molecule reacts with an atom coming from the gas phase [100]. This mechanism should be the dominant surface recombination process for the wall temperature used during the experiments (323 K) [104].

The measurements in pure O_2 plasma [59] show higher loss probabilities, ranging from 3 to 10 $\times$ 10^{-4}, which according to equation (16) is partly due to the lower gas temperatures in O_2 plasmas but specially due to the higher observed loss frequencies [59]. As an example, at 2 Torr 40 mA $\nu_O^{loss\ O_2} - \nu_O^{loss\ CO_2} \sim 14.2\ s^{-1}$ and at 5 Torr 40 mA is $\sim 22.3\ s^{-1}$, where the ratio reaches its maximum $\nu_O^{loss\ O_2}/\nu_O^{loss\ CO_2} \sim 2$). In the literature, only one example has been found comparing γ_O ($\propto \nu_O^{loss}$) for CO_2 and O_2 measured in the same conditions (at 0.005 Torr, in a 300W RF plasma ignited in a helicon reactor), where the ratio $\gamma_O^{O_2}/\gamma_O^{CO_2}$ was $\sim$ 3.75 [50]. A comparison of our results in CO_2 with other γ_O in O_2 plasma literature is difficult because these values are very much dependent on the surface conditions and experimental details as discussed previously, which explain the large dispersion of values published for O_2 plasmas.

A possible explanation for the lower recombination probability in CO_2 than O_2 could be that some of the adsorption sites are occupied by CO_{ads} and not only by O_{ads}. The possibility of CO adsorbed in the walls was already suggested by Cenian *et al.* [41], where the rate for the O+O recombination at the wall is dependent on the CO concentration in the gas phase (reaction 11 in table 1) arguing that the adsorption of CO on the walls was higher than the adsorption of oxygen, being therefore a limiting factor for that reaction. Similarly, lower O densities were found in pure O_2 plasmas compared with O_2 + small amounts of fluorinated compounds, which was explained by the passivation of the surface by F atoms in [121].

There are three possible reactions competing at the wall, $O + O_{ads} \rightarrow O_2$, $CO + O_{ads} \rightarrow CO_2$ and $O + CO_{ads} \rightarrow CO_2$. There is very little information in the literature about the reactions between adsorbed O or CO with atoms or molecules from the gas phase. Loss probabilities have been given for $O_{ads} + O \rightarrow O_2$ and $O_{ads} + CO \rightarrow CO_2$ in [27, 122] obtained in different experimental conditions (higher temperatures, 3000-7000K, simulating entry into the Martian atmosphere). In these works, the loss probability given for $O_{ads} + CO \rightarrow CO_2$ is claimed to be higher than for $O_{ads} + O \rightarrow O_2$.

$$O_{ads} + CO \rightarrow CO_2 \qquad \gamma = 0.15 \cdot exp\left(-15^{(kJ/mol)}/RT_{wall}\right)$$

$$O_{ads} + O \rightarrow O_2 \qquad \gamma = 0.15 \cdot exp\left(-25^{(kJ/mol)}/RT_{wall}\right)$$

Extrapolated to our temperatures, the proposed expression for $O_{ads} + CO \rightarrow CO_2$ gives values between 1.5 and 2 times lower than our results. However the probabilities given for $O_{ads} + O \rightarrow O_2$ in [122] are very low, ~10 times lower than our values. In addition, if the reaction $O_{ads} + CO \rightarrow CO_2$ was the dominant surface recombination process, the densities of O and CO would be more comparable. Therefore, although the probability given for

$O_{ads} + CO \rightarrow CO_2$ could be compatible with out results, the probability for $O_{ads} + O \rightarrow O_2$ should be necessarily higher. There is no information in these works about the reaction with adsorbed CO ($CO_{ads} + O \rightarrow CO_2$) but this is probably not either the dominant process for the same reason mentioned above.

The activation energy obtained, ∼0.1025 eV is slightly lower than the value observed for a pure oxygen plasma ∼0.13 eV [59]. The reason for this is not clear yet; hypothesis include an extra energy contribution, for example from vibrational excited molecules from the gas phase (the vibrational temperatures reported [54] for CO_2 or CO reach 1000K for the asymmetric stretch vibrational mode of CO_2 and 1500K for CO, ∼0.086 eV and 0.13 eV, respectively) or even from the surface itself [46]. More experiments and a comparison with a detailed model of the surface kinetics can help to assess the role of the different adsorbed species on the surface recombination of O atoms in CO_2 plasmas.

For pressures below 1 Torr the data does not show a clear trend with the gas temperature and the loss frequency increases dramatically. This suggests that below 1 Torr we could have plasma enhanced surface recombination processes. Below 1 Torr, the ion collision frequency is reduced causing an increase of the mean energy of ions reaching the wall with decreasing pressure. Therefore the ion bombardment, causing the creation of more chemisorption sites where recombination can occur, could increase the recombination probability for lower pressure as suggested for the case of pure oxygen plasmas [59, 102]. This would also be consistent with the high loss frequency values seen in [50], where CO_2 plasmas at very low pressures (0.005 Torr) were investigated during discharge and post discharge on a Pyrex surface. The loss probability in both cases was very similar, and very high compared to our loss probability under plasma exposure. On the other hand, some contribution from the Langmuir-Hishelwood recombination mechanism cannot be completely discarded, since for the lower pressures T_{gas} is lower and therefore the gas temperature near the wall is closer to the temperature of the cooling system (323K). At this temperature, according to [100, 104], the Eley-Rideal mechanism is indeed still dominant but LH starts to contribute to the total loss probability.

7 Summary and conclusions

The work presented here is part of a series of studies aiming to provide a detailed description of the kinetics of CO_2 plasmas. The measurements provide both the absolute densities and the loss frequencies of the oxygen atoms under conditions for which the densities of CO and CO_2 were also determined. Particular attention was paid to the measurement and data processing methods used, in particular through a detailed comparison between actinometric and HR-TALIF measurements. Several conclusions can be made concerning the experimental methods and the values obtained.

Actinometry and TALIF were used to obtain the O atom densities and were found to give consistent results with regard to the variation as a function of pressure and current. However absolute densities obtained with TALIF tend to be higher than values obtained with actinometry when TALIF data are analysed using the only value of the two-photon absorption cross section of Xe available in the literature, which is a measurement of the ratio between the Xe and oxygen cross sections. When using a recent preliminary value of Xe cross section directly measured by absorption [83], both TALIF and actinometry give consistent absolute atomic oxygen densities. The two oxygen emission lines used for actinometry give also consistent results.

In the case of TALIF, we have found that the TALIF profile (scanning over wavelength) and the TALIF fluorescence (fixing the wavelength at the peak of resonance) give comparable results. We can conclude that there is no need to scan wavelength to obtain absolute densities of reactive atoms, and it is enough to apply a correction factor for the Doppler broadening (and/or pressure broadening for higher pressures) and take into account the isotopic contribution, if needed. This can be useful in terms of experiment efficiency, and allows to disregard the complex isotopic/fine structure present in species such as Xe, or similar, commonly used for absolute calibrations. The high spectral resolution of the laser used allowed us to partially resolve the fine structure of the oxygen profile. This profile was distorted with a focussed beam, probably due to J-dependent photo-ionization processes leading to incorrect gas temperature and O atom density values.

The gas temperature was determined from the Doppler broadening of the TALIF signal for the first time in CO_2 adopting the same procedure previously used in O_2 plasma [60]. The values obtained were found to be very consistent with those extracted from the rotational structure of CO_2 measured by FTIR absorption. The small differences observed are believed to be only due to the different regions sampled by TALIF and IR beams.

The atomic oxygen absolute densities were measured *in situ* for various currents and pressures, giving densities in the order of 1-5 $\times 10^{21}$ m^{-3}. Both actinometry and TALIF have uncertainties, mostly related to the cross sec-

tions used, that prevent from giving these densities with less than 30% error. In any case O atoms represent between 10 to 40% of the CO density which means that atomic oxygen represents a large proportion of the total gas composition in our conditions. This offers an ideal case to study the influence of O atoms on the CO_2 and CO vibrational kinetics in a future work.

The variation of the CO and O densities as a function of the specific energy input, are remarkably different in the pressure range studied here. The CO_2 dissociation fraction quantified by the CO density increases with the SEI and in the first order seems to be well described by the direct electronic impact dissociation rate calculated using the cross section from Polak [110]. However the behaviour at low SEI as well as the saturation of CO obtained at high current for pressures above 1 Torr illustrate that more complex mechanisms need to be taken into account to fully describe the processes that contribute to the CO_2 dissociation.

The O atom densities are shown to strongly depend on surface loss processes in our experimental conditions. Two clearly differentiated regimes were found in the range of pressures studied:

- At low pressures (below 1 Torr) the oxygen atom density increases with pressure. This is the consequence of both the increase of production rate with higher gas density along with the increase of electron density, and the decrease of the surface loss frequency. In this low pressure range, the surface loss probability appears to be enhanced by ion bombardment.

- At pressures above 1 Torr the oxygen atom density decreases with increased pressure, while the loss frequency increases with both pressure and current. The surface loss probability, derived from the loss frequency, shows an Arrhenius dependence with temperature, suggesting a dominant loss process based on surface recombination through an Eley-Rideal mechanism.

This behaviour is similar to that found in pure O_2 plasma. However, the values of loss probabilities derived are quite different, being more than two times lower in CO_2. Adsorbed species, such as CO or CO_2, seem to play an important role inhibiting the O atom recombination in CO_2 plasmas, leading to relatively high O atom density values.

The role of CO and CO_2 molecules in surface mechanisms is certainly an important aspect to study for a better control of O atoms reactivity in CO_2 plasma conversion. The γ_O values provided here for Pyrex exposed to CO_2 plasma and compared to values obtained in pure O_2 plasma in similar conditions give a unique set of data for investigating surface mechanisms induced by CO_2 plasma, which can be of interest for plasma/catalysis, as well as planetary atmosphere entry or polymer processing. The data shown in this work suggest that understanding and controlling the density of adsorbed molecules would be an interesting way to control the amount of oxygen in catalyst/surface driven CO_2 plasma conversion. This could help to reduce the gas phase back reaction between CO and oxygen and to increase the overall efficiency of the process. The role of vibrationally excited species, including vibrationally excited CO, which may have enhanced reaction rates with oxygen atoms, in both gas phase or surface processes remains unknown and should be addressed in future work since almost no experimental data exists for this effect.

8 Acknowledgments

This work was funded by LabEx Plas@par receiving financial aid from the French National Research Agency (ANR) under project SYCAMORE, reference ANR-16-CE06-0005-01. C. Drag was partially funded by LabEx PALM, as part of ANR Investissements d'Avenir under reference ANR-10-LABX-0039-PALM. V. Guerra was partially funded by the Portuguese FCT (Fundaçao para a Ciência e a Tecnologia) under projects UID/FIS/50010/2013 and PTDC/FIS-PLA/1420/2014 (PREMiERE). We would also like to acknowledge Dmitry Lopaev for interesting discussions, Sergey Zyrianov, who developed the Labview programs used during the experiments, and Abhyuday Chatterjee, Bart Klarenaar and Marija Grofulović for their help on different topics related to this paper.

References

[1] Stocker T, Qin D, Plattner G, Tignor M, Allen S, Boschung J, Nauels A, Xia Y, Bex V and Midgley P M 2013 Climate change 2013: The Physical Science Basis. Contribution of Working Group I to the Fifth Assessment Report of the Intergovernmental Panel on Climate Change (IPCC)

[2] Fridman A 2008 Plasma Chemistry (Cambridge University Press)

[3] Spencer L F and Gallimore A D 2011 Plasma Chemistry and Plasma Processing **31**, 79–89

[4] Premathilake D, Outlaw R A, Quinlan R A and Byvik C E 2019 Earth and Space Science

[5] Huang Q, Zhang D, Wang D, Liu K and Kleyn A W 2017 Journal of Physics D: Applied Physics **50**, 294001

[6] Yang R, Zhang D, Zhu K, Zhou H, Ye X, Kleyn A W, Hu Y and Huang Q 2018 Acta Physico-Chimica Sinica **35**, 292–298

[7] Heijkers S, Snoeckx R, Kozak T, Silva T, Godfroid T, Britun N, Snyders R and Bogaerts A 2015 The Journal of Physical Chemistry C **119**, 12815–12828

[8] Silva T, Britun N, Godfroid T and Snyders R 2014 Plasma Sources Science and Technology **23**, 025009

[9] den Harder N, van den Bekerom D C, Al R S, Graswinckel M F, Palomares J M, Peeters F J, Ponduri S, Minea T, Bongers W A and van de Sanden M C 2017 Plasma Processes and Polymers **14**, 1600120

[10] Bongers W, Bouwmeester H, Wolf B, Peeters F, Welzel S, van den Bekerom D, den Harder N, Goede A, Graswinckel M and Groen P W 2017 Plasma processes and polymers **14**, 1600126

[11] Nunnally T, Gutsol K, Rabinovich A, Fridman A, Gutsol A and Kemoun A 2011 Journal of Physics D: Applied Physics **44**, 274009

[12] Wang W, Mei D, Tu X and Bogaerts A 2017 Chemical Engineering Journal **330**, 11–25

[13] Aerts R, Snoeckx R and Bogaerts A 2014 Plasma Processes and Polymers **11**, 985–992

[14] Brehmer F, Welzel S, Van De Sanden M and Engeln R 2014 Journal of Applied Physics **116**, 123303

[15] Duan X, Li Y, Ge W and Wang B 2015 Greenhouse Gases: Science and Technology **5**, 131–140

[16] Taylan O and Berberoglu H 2014 Plasma Sources Science and Technology **24**, 015006

[17] Bak M S, Im S K and Cappelli M 2015 IEEE Transactions on Plasma Science **43**, 1002–1007

[18] Scapinello M, Martini L, Dilecce G and Tosi P 2016 Journal of Physics D: Applied Physics **49**, 075602

[19] Snoeckx R and Bogaerts A 2017 Chemical Society Reviews **46**, 5805–5863

[20] Britun N and Silva T 2018 Plasma Chemistry and Gas Conversion (IntechOpen) ISBN 9781789848403

[21] Qin Y, Niu G, Wang X, Luo D and Duan Y 2018 Journal of CO2 Utilization **28**, 283–291

[22] Medard N, Soutif J C and Poncin-Epaillard F 2002 Surface and Coatings Technology **160**, 197–205

[23] Gancarz I, Poźniak G and Bryjak M 1999 European Polymer Journal **35**, 1419–1428

[24] Fahmy A and Schönhals A 2016 Plasma Processes and Polymers **13**, 499–508

[25] Herdrich G, Auweter-Kurtz M, Kurtz H, Laux T and Winter M 2002 Journal of Thermophysics and Heat Transfer **16**, 440–449

[26] Kolesnikov A F, Pershin I S, Vasil' S A, evskii and Yakushin M I 2000 Journal of spacecraft and rockets **37**, 573–579

[27] Bykova N, Vasilevskii S, Gordeev A, Kolesnikov A F, Fershin I and Yakushin M 1997 Fluid dynamics **32**, 876–886

[28] Marieu V, Reynier P, Marraffa L, Vennemann D, De Filippis F and Caristia S 2007 Acta Astronautica **61**, 604–616

[29] Vacher D, da Silva M L, André P, Faure G and Dudeck M 2008 Plasma Sources Science and Technology **17**, 035012

[30] Lin X, Chen L, Li J, Li F and Yu X 2017 Journal of Thermophysics and Heat Transfer **32**, 503–513

[31] Wu D, Outlaw R and Ash R 1996 Journal of Vacuum Science & Technology A: Vacuum, Surfaces, and Films **14**, 408–414

[32] Guerra V, Silva T, Ogloblina P, Grofulović M, Terraz L, da Silva M L, Pintassilgo C D, Alves L L and Guaitella O 2017 Plasma Sources Science and Technology **26**, 11LT01

[33] Kozák T and Bogaerts A 2014 Plasma Sources Science and Technology **23**, 045004

[34] Buchwald M and Wolga G 1975 The Journal of Chemical Physics **62**, 2828–2832

[35] Cramp J and Lambert J 1973 Chemical Physics Letters **22**, 146–149

[36] Spiridonov M V, McKenna-Lawlor S and Savinov S Y 1994 Journal of Quantitative Spectroscopy and Radiative Transfer **52**, 621–630

[37] Vesel A, Mozetic M, Drenik A and Balat-Pichelin M 2011 Chemical Physics **382**, 127–131

[38] Balat-Pichelin M, Iacono J and Boubert P 2016 Ceramics International **42**, 2761–2769

[39] Sepka S, Chen Y K, Marschall J and Copeland R A 2000 Journal of Thermophysics and Heat Transfer **14**, 45–52

[40] Afonina N, Gromov V and Kovalev V 2002 Fluid dynamics **37**, 117–125

[41] Cenian A, Chernukho A, Borodin V and Śliwiński G 1994 Contributions to Plasma Physics **34**, 25–37

[42] Byron S R and Apter H 1992 Journal of applied physics **71**, 1976–1991

[43] Otorbaev D 1995 Chemical physics **196**, 543–550

[44] Cenian A, Chernukho A and Borodin V 1995 Contributions to Plasma Physics **35**, 273–296

[45] Lopez-Puertas M and Taylor F W 2001 Non-LTE Radiative Transfer in the Atmosphere (WORLD SCIENTIFIC)

[46] Armenise I and Kustova E 2018 The Journal of Physical Chemistry A

[47] Chen G, Britun N, Godfroid T, Georgieva V, Snyders R and Delplancke-Ogletree M P 2017 Journal of Physics D: Applied Physics **50**, 084001

[48] Michielsen I, Uytdenhouwen Y, Pype J, Michielsen B, Mertens J, Reniers F, Meynen V and Bogaerts A 2017 Chemical Engineering Journal **326**, 477–488

[49] Jafarzadeh A, Bal K M, Bogaerts A and Neyts E C 2019 The Journal of Physical Chemistry C **123**, 6516-6525

[50] Bousquet A, Cartry G and Granier A 2007 Plasma Sources Science and Technology **16**, 597

[51] Magne L, Coitout H, Cernogora G and Gousset G 1993 Journal de Physique III **3**, 1871–1889

[52] Cartry G, Magne L and Cernogora G 2000 Journal of Physics D: Applied Physics **33**, 1303

[53] Klarenaar B, Engeln R, van den Bekerom D, van de Sanden M, Morillo-Candas A S and Guaitella O 2017 Plasma Sources Science and Technology **26**, 115008

[54] Klarenaar B L M, Morillo-Candas A S, Grofulović M, van de Sanden M C M, Engeln R and Guaitella O 2019 Plasma Sources Science and Technology **28**, 035011

[55] Silva T, Grofulović M, Klarenaar B, Morillo-Candas A, Guaitella O, Engeln R, Pintassilgo C and Guerra V 2018 Plasma Sources Science and Technology **27**, 015019

[56] Grofulović M, Silva T, Klarenaar B L M, Morillo-Candas A S, Guaitella O, Engeln R, Pintassilgo C D and Guerra V 2018 Plasma Sources Science and Technology **27**, 115009

[57] Klarenaar B, Grofulović M, Morillo-Candas A S, van den Bekerom D, Damen M, Van De Sanden M, Guaitella O and Engeln R 2018 Plasma Sources Science and Technology **27**, 045009

[58] Lopaev D and Smirnov A 2004 Plasma physics reports **30**, 882–893

[59] Booth J P, Guaitella O, Chatterjee A, Drag C, Guerra V, Lopaev D, Zyryanov S M, Rakhimova T V, Voloshin D and Mankelevich Y A 2019 Plasma Sources Science and Technology

[60] Booth J P, Marinov D, Foucher M, Guaitella O, Bresteau D, Cabaret L and Drag C 2015 Journal of Instrumentation **10**, C11003

[61] Marinov D, Drag C, Blondel C, Guaitella O, Golda J, Klarenaar B, Engeln R, Schulz-von der Gathen V and Booth J P 2016 Plasma Sources Science and Technology **25**, 06LT03

[62] Cabaret L and Drag C 2010 The European Physical Journal-Applied Physics **51**

[63] Lottigier P, Jucha A, Cabaret L, Blondel C and Drag C 2019 Applied Physics B **125**, 14

[64] Coburn J and Chen M 1980 Journal of applied physics **51**, 3134–3136

[65] Pagnon D, Amorim J, Nahorny J, Touzeau M and Vialle M 1995 Journal of Physics D: Applied Physics **28**, 1856

[66] Hagelaar G and Pitchford L 2005 Plasma Sources Science and Technology **14**, 722

[67] Tsutsumi T, Greb A, Gibson A R, Hori M, O'Connell D and Gans T 2017 Journal of Applied Physics **121**, 143301

[68] Laher R R and Gilmore F R 1990 Journal of Physical and Chemical Reference Data **19**, 277–305

[69] Schulman M B, Sharpton F A, Chung S, Lin C C and Anderson L 1985 Physical review A **32**, 2100

[70] Puech V and Tonhin L 1986 Journal of Physics D: Applied Physics **19**, 2309-23

[71] IST-lisbon database, www.lxcat.net, retrieved on 16 august, 2018

[72] Guerra V *et al* 2019 Cross sections for CO electron impact excitation. IST-Lisbon database. *Private communication*

[73] Kramida A, Yu Ralchenko, Reader J and and NIST ASD Team 2018 NIST Atomic Spectra Database (ver. 5.5.6), [Online]. Available: `https://physics.nist.gov/asd` [2018, August 30]. National Institute of Standards and Technology, Gaithersburg, MD.

[74] Nick K and Helbig V 1984 Physica Scripta **1984**, 100

[75] Niemi K, Schulz-Von Der Gathen V and Döbele H 2005 Plasma Sources Science and Technology **14**, 375

[76] Dagdigian P J, Forch B E and Miziolek A W 1988 Chemical Physics Letters **148**, 299 - 308

[77] Sadeghi N, Setser D, Francis A, Czarnetzki U and Döbele H 2001 The Journal of Chemical Physics **115**, 3144–3154

[78] Kunze H J 2009 Introduction to plasma spectroscopy vol 56 (Springer Science & Business Media)

[79] Amorim J, Baravian G and Jolly J 2000 Journal of Physics D: Applied Physics **33**, R51

[80] Amorim J and Baravian G 2001 Optics communications **192**, 277–286

[81] Bamford D J, Jusinski L E and Bischel W K 1986 Physical Review A **34**, 185

[82] Goehlich A, Kawetzki T and Döbele H 1998 The Journal of chemical physics **108**, 9362–9370

[83] Drag C *et al* 2018 Direct measurement of two-photon excitation cross section of Xe by absorption. *Presented in the 8th International Workshop on Plasma Spectroscopy (IPS), 2018*

[84] Aymar M and Coulombe M 1978 Atomic Data and Nuclear Data Tables **21**, 537–566

[85] Horiguchi H, Chang R and Setser D 1981 The Journal of Chemical Physics **75**, 1207–1218

[86] Saxon R P and Eichler J 1986 Physical Review A **34**, 199

[87] Amorim J, Baravian G and Sultan G 1996 Applied physics letters **68**, 1915–1917

[88] Marinov D, Booth J, Drag C and Blondel C 2017 Journal of Physics B: Atomic, Molecular and Optical Physics **50**, 065003

[89] Kono M, He Y, Baldwin K G and Orr B J 2016 Journal of Physics B: Atomic, Molecular and Optical Physics **49**, 065002

[90] Saloman E B 2004 Journal of Physical and Chemical Reference Data **33**, 765-921

[91] Grofulović M, Klarenaar B L M, Guaitella O, Guerra V and Engeln R 2019 Plasma Sources Science and Technology

[92] Raizer Y P 1991 Gas discharge physics (Springer)

[93] Niemi K, Schulz-Von Der Gathen V and Döbele H 2001 Journal of Physics D: Applied Physics **34**, 2330

[94] Katsch H, Tewes A, Quandt E, Goehlich A, Kawetzki T and Döbele H 2000 Journal of Applied Physics **88**, 6232–6238

[95] Guaitella O *et al* 2019 Investigating CO_2 plasma kinetics with in situ infrared absorption Fourier transformed spectroscopy and complementary diagnostics. *Presented in the 13th Frontiers in Low-Temperature Plasma Diagnostics (FLTPD), 2019*

[96] Balat-Pichelin M and Beche E 2010 Applied Surface Science **256**, 4906–4914

[97] Paterna D, Monti R, Savino R and Esposito A 2002 Journal of spacecraft and rockets **39**, 227–236

[98] Pekakovic D A, Marschall J, Duan L and Martin M P 2008 Journal of Thermophysics and Heat Transfer **22**, 178–186

[99] Wickramanayaka S, Hosokawa N and Hatanaka Y 1991 Japanese journal of applied physics **30**, 2897

[100] Kim Y C and Boudart M 1991 Langmuir **7**, 2999–3005

[101] Greaves J and Linnett J 1959 Transactions of the Faraday Society **55**, 1355–1361

[102] Cartry G, Duten X and Rousseau A 2006 Plasma Sources Science and Technology **15**, 479

[103] Cartry G, Magne L and Cernogora G 1999 Journal of Physics D: Applied Physics **32**, L53

[104] Macko P, Veis P and Cernogora G 2004 Plasma Sources Science and Technology **13**, 251

[105] Marinov D, Guerra V, Guaitella O, Booth J P and Rousseau A 2013 Plasma Sources Science and Technology **22**, 055018

[106] Balat-Pichelin M, Badie J, Berjoan R and Boubert P 2003 Chemical Physics **291**, 181–194

[107] Bedra L and Balat-Pichelin M J 2005 Aerospace Science and Technology **9**, 318–328

[108] Bedra L, Rutigliano M, Balat-Pichelin M and Cacciatore M 2006 Langmuir **22**, 7208–7216

[109] Lopaev D, Malykhin E and Zyryanov S 2010 Journal of Physics D: Applied Physics **44**, 015201

[110] Polak L and Slovetsky D 1976 International Journal for Radiation Physics and Chemistry **8**, 257–282

[111] Sabadil H and Pfau S 1985 Plasma chemistry and plasma processing **5**, 67–79

[112] Lopaev D, Malykhin E and Zyryanov S 2010 Journal of Physics D: Applied Physics **44**, 015202

[113] ETH Zurich, High Voltage Laboratory database, www.lxcat.net, retrieved on September 27, 2018.

[114] Grofulović M, Alves L L and Guerra V 2016 Journal of Physics D: Applied Physics **49**, 395207

[115] Morillo-Candas A S, Guerra V and Guaitella O 2019 In preparation

[116] Guerra V 2007 IEEE Transactions on plasma science **35**, 1397–1412

[117] Beuthe T G and Chang J S 1997 Japanese Journal of applied physics **36**, 4997

[118] Slovetsky D I 1980 Chemical reactions mechanisms in nonequilibrium plasmas (Nauka, Moscow (in russian))

[119] Chantry P 1987 Journal of applied physics **62**, 1141–1148

[120] Mehio N, Dai S and Jiang D e 2014 The Journal of Physical Chemistry A **118**, 1150–1154

[121] Booth J and Sadeghi N 1991 Journal of applied physics **70**, 611–620

[122] Kovalev V, Afonina N and Gromov V 2005 Heat transfer modelling to catalytic protection systems of space vehicles entering into martian atmosphere Shock Waves (Springer) pp 597–602